


Spin and quadrupole correlations by three-spin interaction in the frustrated pyrochlore magnet $\text{Tb}_{2+x}\text{Ti}_{2-x}\text{O}_{7+y}$

Hiroaki Kadowaki  and Mika Wakita*Department of Physics, Tokyo Metropolitan University, Hachioji, Tokyo 192-0397, Japan*

Björn Fåk and Jacques Ollivier

Institut Laue-Langevin, CS 20156, 38042 Grenoble Cedex 9, France

Seiko Ohira-Kawamura

Neutron Science Section, MLF, J-PARC Center, Shirakata, Tokai, Ibaraki 319-1195, Japan (Received 17 September 2021; revised 21 December 2021; accepted 3 January 2022; published 28 January 2022)

We have investigated the origin of the magnetic dipole correlations $\langle \sigma_{\mathbf{Q}}^z \sigma_{-\mathbf{Q}}^z \rangle$ characterized by the modulation wave vector $\mathbf{k} \sim (\frac{1}{2}, \frac{1}{2}, \frac{1}{2})$ observed in the frustrated pyrochlore magnet $\text{Tb}_{2+x}\text{Ti}_{2-x}\text{O}_{7+y}$. This magnetic short-range order cannot be accounted for by adding further-neighbor exchange interactions to the nearest-neighbor pseudospin- $\frac{1}{2}$ Hamiltonian for quantum pyrochlore magnets. Using classical Monte Carlo simulation and quantum simulation based on thermally pure quantum (TPQ) states we have shown that the spin correlations with $\mathbf{k} \sim (\frac{1}{2}, \frac{1}{2}, \frac{1}{2})$ are induced at low temperatures by a three-spin interaction of a form $\sigma_r^\pm \sigma_r^z \sigma_{r'}^\pm$, which is a correction to the Hamiltonian due to the low crystal-field excitation. Simulations using TPQ states have shown that the spin correlations coexist with electric quadrupole correlations $\langle \sigma_{\mathbf{Q}}^\alpha \sigma_{-\mathbf{Q}}^\beta \rangle$ ($\alpha, \beta = x, y$) with $\mathbf{k} \sim \mathbf{0}$. These results suggest that the putative quantum spin liquid state of $\text{Tb}_{2+x}\text{Ti}_{2-x}\text{O}_{7+y}$ is located close to phase boundaries of the spin-ice, quadrupole-ordered, and magnetic-ordered states in the classical approximation, and that the three-spin interaction brings about a quantum disordered ground state with both spin and quadrupole correlations.

DOI: [10.1103/PhysRevB.105.014439](https://doi.org/10.1103/PhysRevB.105.014439)

I. INTRODUCTION

Frustrated magnetic systems have been actively studied in decades [1]. Archetypal frustrated systems consist of spins or pseudospins residing on lattices built from triangular and tetrahedral units. For example, antiferromagnetically coupled Ising spins on a tetrahedron are prohibited from possessing a simple ground-state configuration, being referred to as geometrical frustration. Geometrically frustrated classical and quantum magnets on two-dimensional (2D) triangle [2–4] and kagome [5–7] lattices, and three-dimensional (3D) pyrochlore-lattice systems [8–11] have been investigated. Among frustrated classical magnets, the spin ice on a pyrochlore lattice is of crucial importance because of its macroscopically degenerate ground-state [10] and fractionalized magnetic monopole excitations [12–16]. Possibilities of quantum spin liquid (QSL) states in frustrated magnets have been actively studied in a number of years [17,18]. By introducing transverse interactions in a frustrated Ising system, a QSL ground state without conventional magnetic long-range order (LRO) can occur, which provides challenging theoretical problems [19,20]. Investigations of real (or candidate) QSL magnets are fascinating experimental explorations [4,7,21–23].

A non-Kramers pyrochlore magnet $\text{Tb}_2\text{Ti}_2\text{O}_7$ has attracted much attention for decades as a QSL candidate [9,11]. For this system, any conventional magnetic LRO has never been

reported. However, our careful studies using off-stoichiometry controlled samples $\text{Tb}_{2+x}\text{Ti}_{2-x}\text{O}_{7+y}$ (TTO) [24–26] showed that TTO samples in the range $x > x_c \simeq -0.0025$ have a ground state with a conventional LRO with a hidden order parameter. We proposed that this LRO is an electric quadrupole (or multipole) order [27–29], which was predicted for general non-Kramers pyrochlore f -electron magnets [30–32]. Recently, an ultrasound experiment proved more firmly that a phase transition from the paramagnetic state to a quadrupole-ordered (QO) state actually occurs [33]. On the other hand, for TTO samples in the range $x < x_c$ we showed that they have a disordered ground state without any conventional LRO [24–26,34], being the putative QSL ground state of TTO debated in many years [11,35]. In spite of these experimental advances, theoretical challenges of clarifying the nature of this disordered ground state remain very difficult to date [35].

One can naturally expect that the QSL state of TTO can be understood within a framework of the pseudospin- $\frac{1}{2}$ nearest-neighbor (NN) exchange Hamiltonian [Eq. (1)] for non-Kramers pyrochlore magnets [30,31]. In this understanding it is referred to as a U(1) QSL state [19,32] or the quantum spin-ice (QSI) state [36,37]. However, it is not obvious whether the state in question is really the QSI state (or a state adiabatically connected to QSI) or another disordered ground state. From an experimental viewpoint there are at least two observed facts which do not conform to the QSI state, posing two problems to be solved.

The first problem is why specific heat of QSL samples of TTO ($x < x_c$) behaves almost temperature independent, $C(T) \sim \text{const}$ in a range $T < 2$ K [24], while for the QSI model $C(T)$ shows the single-peak structure (anticipated at $T \sim 1$ K for TTO), which is a characteristic of the classical spin-ice model and appears also in QSI [38]. To resolve this problem, the effective Hamiltonian of TTO has to be determined more precisely than that proposed in our previous study [27], and a theoretical model calculation has to be performed. It seems that an important term is absent in our proposed Hamiltonian [27].

The second problem is why spin correlations observed by neutron scattering experiments show pronounced magnetic short-range order (SRO) close to the wave vector $\mathbf{k} \sim (\frac{1}{2}, \frac{1}{2}, \frac{1}{2})$ [34], while for the QSI model spin correlations show the pinch-point-like structure at $\mathbf{k} \sim \mathbf{0}$ [38], that is commonly seen in spin-ice models. In order to solve this problem, we studied a simple hypothesis that magnetic further-neighbor exchange interactions would modify the spin correlations by lifting the spin-ice degeneracy. But we had to reject this naive hypothesis because unrealistically further-neighbor interactions were required to reproduce the observed spin correlations [34].

In this study, to solve the second problem we attempt to make use of another hint from an experimental fact that QO samples of TTO show a very small magnetic LRO with $\mathbf{k} = (\frac{1}{2}, \frac{1}{2}, \frac{1}{2})$, where the magnitude of the ordered moment is as small as $\sim 0.1\mu_B$, which is much smaller than the moment $\simeq 5\mu_B$ of the crystal-field (CF) ground-state doublet [24,27,34,39]. If this is an intrinsic effect, one can come up with an idea that there is a weak interaction term in the Hamiltonian which couples magnetic dipole and electric quadrupole degrees of freedom. This coupling term may be at work, thereby spin and quadrupole correlations (and LRO) develop and affect each other at low temperatures.

This kind of weak interaction was theoretically pointed out to exist as a three-spin interaction term in TTO and generally in non-Kramers pyrochlore magnets with low CF excited states [35,40]. This interaction is derived from a perturbation expansion via virtual CF excitations [40]. To date, however, few investigations focusing on the three-spin interaction have been carried out. In this study, we explore a possibility that the observed spin correlations with $\mathbf{k} \sim (\frac{1}{2}, \frac{1}{2}, \frac{1}{2})$ are accounted for by adding the three-spin interaction term to the NN bilinear Hamiltonian [Eq. (1)]. More specifically, we compare the structure factor $S(\mathbf{Q}) = \int S(\mathbf{Q}, E) dE$, where $S(\mathbf{Q}, E)$ is the dynamic structure factor obtained from our previous inelastic neutron scattering data [26,34], with theoretical model calculations to find appropriate parameters of the three-spin interaction term.

Among theoretical tools of model calculations for frustrated systems we chose two methods. One is the classical Monte Carlo (MC) simulation technique for Heisenberg models [41], which has been expected to be valuable for a phase transition with a finite critical temperature T_c [29,42,43]. The other is a quantum simulation technique based on the typicality of quantum statistical mechanics [44–46] and the thermally pure quantum (TPQ) states [47–49]. Two methods using a microcanonical TPQ (mTPQ) state [48,50] and a canonical TPQ (cTPQ) state [47,49] were employed. These simulation

methods using the TPQ states are useful for frustrated quantum magnets, and have been applied for those on kagome [49,51], honeycomb [52,53], square [54], and pyrochlore [55,56] lattices. They enable approximation-free quantum simulation down to relatively low temperatures for systems as large as those of exact diagonalization. Using these two simulation methods we have found that the spin correlations with $\mathbf{k} \sim (\frac{1}{2}, \frac{1}{2}, \frac{1}{2})$ can be induced by the three-spin interaction.

In the following sections, we summarize effective Hamiltonians, our previous work [27], and a technical target of this study in Sec. II. We present methods of neutron scattering experiments and the simulations in Sec. III, and experimental and simulation results in Sec. IV, which are discussed in Sec. V.

Considering that the simulation technique using the TPQ states has never been applied to analysis of $S(\mathbf{Q})$ observed by neutron scattering and that this technique itself has several limitations, we decide to show a number of figures of calculated $S(\mathbf{Q})$ for careful readers especially who will use this technique for other quantum pyrochlore magnets and who will examine the present results for further theoretical investigations. When these figures are inspected, we recommend using two (or more) displays to maximize the reader's image-recognition-processing ability. For readers who are interested in mainly results of the TTO analysis (and for first-time readers), to spare them the technical details we suggest that they read Sec. II first, and then observe Figs. 5(a0,c0), Fig. 8(k0) (with Fig. 3), and Figs. 13(c1,d1) and 11(a) (with Fig. 1), before proceeding to the Conclusion section.

II. PSEUDOSPIN- $\frac{1}{2}$ HAMILTONIAN

A minimal theoretical model for general non-Kramers f -electron magnets on a pyrochlore lattice [30–32] is the effective pseudospin- $\frac{1}{2}$ Hamiltonian due to electronic superexchange interactions. It is expressed as

$$\mathcal{H}_0 = J_{\text{nn}} \sum_{(r,r')} \sigma_r^z \sigma_{r'}^z + J_{\text{nn}} \sum_{(r,r')} [2\delta(\sigma_r^+ \sigma_{r'}^- + \sigma_r^- \sigma_{r'}^+) + 2q(e^{2i\phi_{r,r'}} \sigma_r^+ \sigma_{r'}^+ + \text{H.c.})], \quad (1)$$

where magnetic dipole and electric quadrupole moments at each site \mathbf{r} are represented by Pauli matrices σ_r^z and $\sigma_r^\pm = (\sigma_r^x \pm i\sigma_r^y)/2$, respectively, which are defined within the CF ground-state doublet. The summation of Eq. (1) runs over NN site pairs (r, r') . Detailed definitions of the Hamiltonian for TTO, the CF ground-state doublet, lattice sites, phases $\phi_{r,r'}$, etc., are described in Appendix A.

The classical phase diagram of the effective Hamiltonian [Eq. (1)] for $J_{\text{nn}} > 0$ at $T = 0$ [31,35] is reproduced in Fig. 1 to briefly explain the results of our previous work of applying Eq. (1) to TTO [27] and a technical target of this investigation. At the origin of Fig. 1, $(\delta, q) = (0, 0)$, the Hamiltonian consists of the first term of Eq. (1) representing the classical spin-ice (SI) model. A spin configuration of the macroscopically degenerate SI state is illustrated in Fig. 1(a). In a region close to the origin ($|\delta|, |q| \ll 1$), the second transverse term of Eq. (1) lifts the macroscopic degeneracy and the system has the U(1) QSL (QSI) ground state [19,31,32]. On the other hand, in regions far from origin ($|\delta| \gg 1$ or

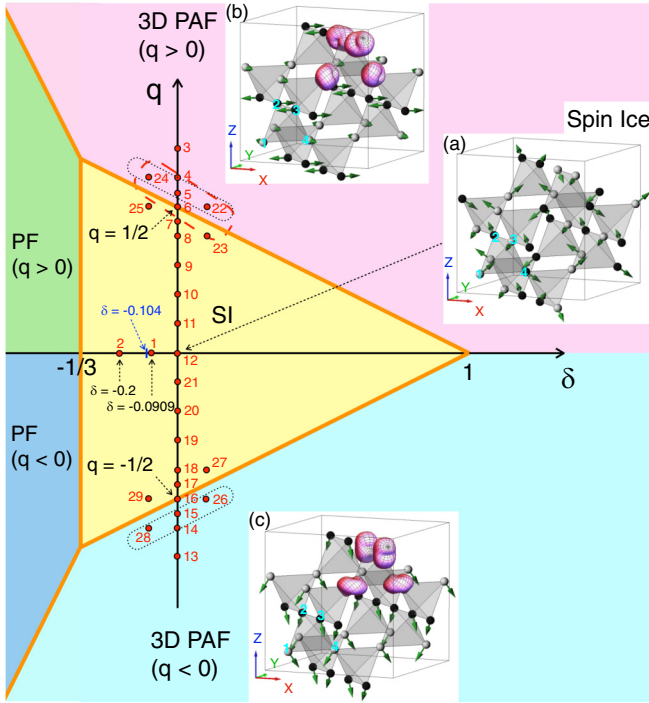


FIG. 1. Classical phase diagram of the effective Hamiltonian \mathcal{H}_0 [Eq. (1)] for $J_{nn} > 0$ at $T = 0$ [31]. Red circles, points 1–29, denote parameter sets of (δ, q) where simulations using the TPQ states were performed. The two regions enclosed by the black dotted lines represent the acceptable parameters for the QO sample of TTO proposed in our previous analyses [27]. The region enclosed by the red dashed line represents the suggested parameters for QO and QSL samples of TTO ($-0.007 < x < 0.003$) by this study. (a) A spin configuration of the classical spin-ice state for $(\delta, q) = (0, 0)$, where $\sigma_{t_n+d_v} = \pm z_v$. (b) A pseudospin configuration of the quadrupole order 3D PAF ($q > 0$) [29], where $\langle \sigma_{t_n+d_v} \rangle = y_v$ ($v = 1, 4$) and $\langle \sigma_{t_n+d_v} \rangle = -y_v$ ($v = 2, 3$), and schematic view of the deformation of the f -electron charge density. (c) A pseudospin configuration of the quadrupole order 3D PAF ($q < 0$), where $\langle \sigma_{t_n+d_v} \rangle = x_v$ ($v = 1, 4$) and $\langle \sigma_{t_n+d_v} \rangle = -x_v$ ($v = 2, 3$), and schematic view of the deformation of the f -electron charge density.

$|q| \gg 1$), there are four classical LRO ground states: 3D planar antiferropseudospin (PAF) ($q > 0$), 3D PAF ($q < 0$), planar ferropseudospin (PF) ($q > 0$), and PF ($q < 0$) using the notations of Refs. [29,31], which correspond to PC, SFM, ψ_2 , and ψ_3 of Ref. [35], respectively. Pseudospin configurations of the 3D-PAF ($q > 0$) and 3D-PAF ($q < 0$) states are shown in Figs. 1(b) and 1(c), respectively, where electric quadrupole (multipole) orders of these states are also illustrated by deformation of the f -electron charge density from the SI state [27–29]. Intermediate states between the QSI and classical LRO states have not been fully studied [32,57,58]. On the negative δ -axis large-scale quantum Monte Carlo simulation was performed [38], which showed that the classical critical point $(\delta, q)_c = (-1/3, 0)$ moves to $(\delta, q)_c = (-0.104, 0)$ for the quantum system.

In the previous study [27], we made arguments based mostly on classical approximations that the QO sample of TTO with $x = 0.005$ is located close to the phase boundary between the SI and 3D-PAF phases. The acceptable (δ, q)

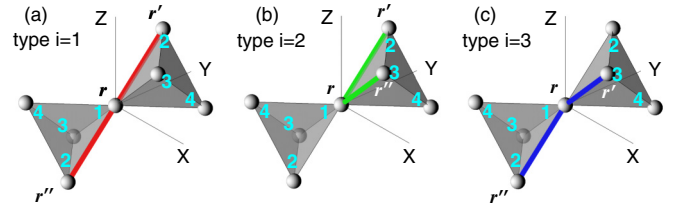


FIG. 2. Three geometrically distinct triplets $\langle r, r', r'' \rangle$ of Eq. (3) are illustrated in (a), (b), and (c), which correspond to the type $i = 1, 2$, and 3 three-spin interaction with the coupling constant $J_{3s,i}$, respectively.

ranges for the QO sample correspond to the two regions enclosed by black dotted lines in Fig. 1 [27]. We note that the pseudospin configuration of the LRO with $q < 0$ is related to that with $q > 0$ by the transformation of rotating σ_r about the local z_r axis by $\pi/2$ [31].

In classical MC (CMC) simulation, we include the magnetic dipolar interaction [27,28] described by

$$\mathcal{H}_d = D r_{nn}^3 \sum \left\{ \frac{z_r \cdot z_{r'}}{|\Delta r|^3} - \frac{3[z_r \cdot \Delta r][z_{r'} \cdot \Delta r]}{|\Delta r|^5} \right\} \sigma_r^z \sigma_{r'}^z, \quad (2)$$

where the summation runs over all pairs of sites, r_{nn} is the NN distance, and $\Delta r = r - r'$. This interaction can be approximated by $D_{nn} \sum_{\langle r, r' \rangle} \sigma_r^z \sigma_{r'}^z$ with $D_{nn} = \frac{5}{3} D$ [59,60]. Thus, the effective Hamiltonian of $\mathcal{H}_0 + \mathcal{H}_d$ can be approximated by \mathcal{H}_0 with replacements $J_{nn} \rightarrow J_{nn} + D_{nn}$, $\delta \rightarrow J_{nn} \delta / (J_{nn} + D_{nn})$, and $q \rightarrow J_{nn} q / (J_{nn} + D_{nn})$.

In addition to \mathcal{H}_0 and \mathcal{H}_d , we consider a three-spin interaction term expressed as

$$\mathcal{H}_{3s} = \sum_{i=1}^3 J_{3s,i} \sum_{\langle r, r', r'' \rangle} [e^{i\phi_{r,r',r''}^{(i)}} \sigma_r^+ \sigma_{r'}^z \sigma_{r''}^z + \text{H.c.}], \quad (3)$$

where $\langle r, r' \rangle$ and $\langle r, r'' \rangle$ are NN pairs and $r' \neq r''$, which are satisfied by three distinct types of triplet $\langle r, r', r'' \rangle$ shown in Fig. 2 [35,40]. By imposing the condition of invariance under the space-group symmetry to \mathcal{H}_{3s} , one can show that the three-spin interaction term has the form of Eq. (3) with three real coupling constants $J_{3s,i}$ ($i = 1, 2, 3$) and phases $\phi_{r,r',r''}^{(i)}$ listed in Tables III–V in Appendix B. We note that the phases $\phi_{r,r',r''}^{(i)}$ ($i = 1, 2, 3$) with the site triplet $\langle r, r', r'' \rangle$ illustrated in Figs. 2(a)–2(c) are listed in the first lines of Tables III–V, respectively. Since the phases $\phi_{r,r',r''}^{(i)}$ are fixed by the symmetry, the adjustable parameters of \mathcal{H}_{3s} are the three coupling constants $J_{3s,i}$.

We used total effective Hamiltonians $\mathcal{H} = \mathcal{H}_0 + \mathcal{H}_d + \mathcal{H}_{3s}$ and $\mathcal{H} = \mathcal{H}_0 + \mathcal{H}_{3s}$ for the classical and quantum simulations, respectively. The magnitude of the coupling constants of $\mathcal{H}_0 + \mathcal{H}_d$, scaled by J_{nn} and D_{nn} , should be close to that of our previous study [27], in which $J_{nn} = 1.0$ K and $D_{nn} = 0.48$ K. As for the parameters (δ, q) , they should be close to one of the two regions enclosed by the black dotted lines in Fig. 1 [27]. Thus, the technical target of this study is to find parameter sets $(J_{3s,1}, J_{3s,2}, J_{3s,3})$ of \mathcal{H}_{3s} which can explain the spin correlations of TTO. The magnitude of $J_{3s,i}$ is the order of $J_{nn}^2 / \Delta \approx 0.1 J_{nn} \approx 0.1$ K, where Δ is the energy of the first CF excited state [35,40]. It should be noted that since the

theoretical tools we applied are far from perfect for many-body quantum states, what we can do best at present would be to qualitatively reproduce the spin correlations of TTO using the simulations.

III. METHODS

A. Experimental methods

Single-crystalline samples of $\text{Tb}_{2+x}\text{Ti}_{2-x}\text{O}_{7+y}$ with $x = -0.007, 0.000, \text{ and } 0.003$ used in this study are those of Refs. [26,34], where methods of the sample preparation and the estimation of x values are described. The QSL sample with $x = -0.007$ remains in the paramagnetic state down to 0.1 K. The QO samples with $x = 0.000$ and 0.003 very likely have small and large electric quadrupole orders, respectively, in $T \ll T_c \sim 0.4$ K [24,25].

Neutron scattering experiments were carried out on the time-of-flight (TOF) spectrometer IN5 operated with $\lambda = 8$ Å at ILL for the $x = -0.007$ and 0.000 crystal samples [26,34,61,62]. The energy resolution of this condition was $\Delta E = 0.021$ meV (FWHM) at the elastic position. Neutron scattering experiments for the $x = 0.003$ crystal sample were performed on the TOF spectrometer AMATERAS operated with $\lambda = 7$ Å at J-PARC [26,34]. The energy resolution of this condition was $\Delta E = 0.024$ meV (FWHM) at the elastic position. Each crystal sample was mounted in a dilution refrigerator so as to coincide its (h, h, l) plane with the horizontal scattering plane of the spectrometer. The observed intensity data were corrected for background and absorption using a home-made program [63]. Construction of a four-dimensional $S(\mathbf{Q}, E)$ data object from a set of the TOF data taken by rotating each crystal sample was performed using HORACE [64].

B. Classical MC simulation

Classical MC simulations of the model described by $\mathcal{H} = \mathcal{H}_0 + \mathcal{H}_d + \mathcal{H}_{3s}$ [Eqs. (1)–(3)] were carried out by treating the pseudospin σ_r as a classical unit vector [41]. The NN exchange constant and the dipole interaction parameter were fixed to $J_{nn} = 1.0$ K and $D_{nn} = 0.48$ K [27]. The parameter sets of (δ, q) were $J_{nn}\delta/(J_{nn} + D_{nn}) = -0.1, 0, 0.1$ and $J_{nn}|q|/(J_{nn} + D_{nn}) + J_{nn}\delta/[2(J_{nn} + D_{nn})] = 1.1/2, 0.9/2$, encompassing the 3D-PAF and classical SI states. These are shown by red circles, the points 31–42, in Fig. 3. The CMC simulations were performed with typically $\sim 4 \times 10^5$ MC steps per spin and on periodic clusters with $N = 16L^3$ spins (sites), where $L (=4, 10)$ stands for a linear dimension parallel to the [100] direction. The MC steps were selected by confirming that further increases of them did not essentially change results. We used the Metropolis single spin-flip update [41] and the exchange Monte Carlo method [65].

C. Quantum simulation using TPQ states

We have adopted methods of the quantum simulation based on the mTPQ and cTPQ states which are described in Refs. [48–50]. These methods enable us to calculate expectation values of observables and thermodynamic quantities

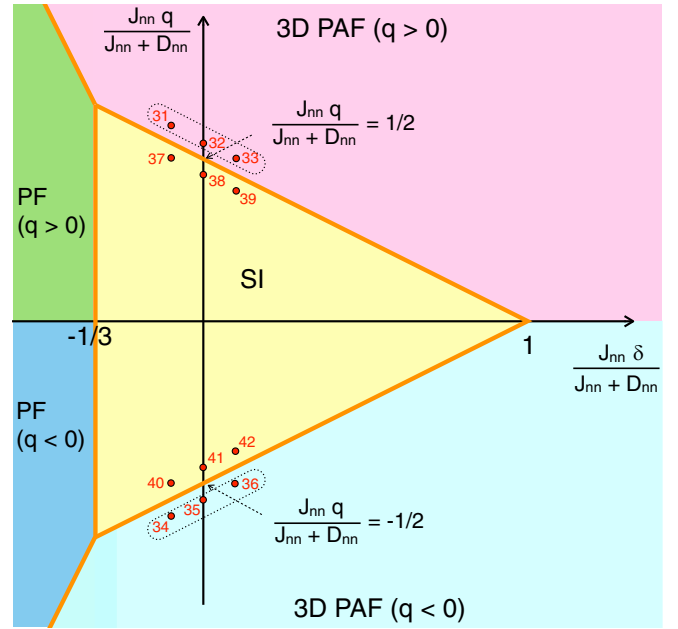


FIG. 3. Classical phase diagram of the effective Hamiltonian $\mathcal{H}_0 + \mathcal{H}_d$ [Eqs. (1) and (2)] where the magnetic dipolar interaction is approximated by the NN coupling $D_{nn} \sum_{(r,r')} \sigma_r^z \sigma_{r'}^z$. Red circles, points 31–42, denote parameter sets of (δ, q) where CMC simulations were performed. The two regions enclosed by the black dotted lines represent the acceptable parameters for the QO sample of TTO proposed in our previous analyses [27].

at finite temperatures by applying a computational technique which is commonly used for the Lanczos method [50,66,67]. The algorithm of the simulation using the mTPQ state can be performed by storing only two vectors in the 2^N -dimensional Hilbert space, where N is the number of pseudospins (sites). It is not difficult to carry out this simulation for a system with $N = 32$ sites without special techniques on a PC with about 160 GB memory. We calculated expectation values of pseudospin correlations and thermodynamic quantities using the methods of the mTPQ and cTPQ states, respectively.

A series of mTPQ states are generated by iteratively operating the Hamiltonian \mathcal{H} to a random normalized vector $|\psi_0\rangle$ in the Hilbert space [48]. More specifically, the mTPQ states are calculated by

$$|\psi_k\rangle = \frac{1}{\sqrt{Q_k}} (\ell - \hat{h})^k |\psi_0\rangle, \quad (4)$$

where $k = 0, 1, 2, \dots$, $\hat{h} = \mathcal{H}/N$, ℓ is a constant larger than the maximum eigenvalue of \hat{h} , and $Q_k = |(\ell - \hat{h})^k |\psi_0\rangle|^2$ is a normalization constant. The temperature corresponding to $|\psi_k\rangle$ is

$$T_k = \frac{N}{2kk_B} (\ell - \langle \psi_k | \hat{h} | \psi_k \rangle). \quad (5)$$

An equilibrium expectation value of an observable represented by an operator \hat{A} for the mTPQ state $|\psi_k\rangle$ is

$$\langle \hat{A} \rangle_k = \langle \psi_k | \hat{A} | \psi_k \rangle. \quad (6)$$

By applying this equation to pseudospin correlations $\hat{A} = \sigma_r^\alpha \sigma_{r'}^\alpha$ ($\alpha = x, z$), the Fourier transform of their expectation

values is calculated by

$$\langle \sigma_{\mathbf{Q}}^{\alpha} \sigma_{-\mathbf{Q}}^{\alpha} \rangle \propto \sum_{r,r'} \langle \sigma_r^{\alpha} \sigma_{r'}^{\alpha} \rangle_k \exp[-i\mathbf{Q} \cdot (\mathbf{r} - \mathbf{r}')]. \quad (7)$$

Similarly, the structure factor $S(\mathbf{Q})$ at T_k is calculated by

$$S(\mathbf{Q}) \propto f(Q)^2 \sum_{r,r'} [z_r \cdot z_{r'} - (\hat{\mathbf{Q}} \cdot z_r)(\hat{\mathbf{Q}} \cdot z_{r'})] \times \langle \sigma_r^z \sigma_{r'}^z \rangle_k \exp[-i\mathbf{Q} \cdot (\mathbf{r} - \mathbf{r}')], \quad (8)$$

where $f(Q)$ is the magnetic form factor and $\hat{\mathbf{Q}} = \mathbf{Q}/|\mathbf{Q}|$. These expectation values [Eqs. (7) and (8)] are averaged over different (typically four) realizations of the series of the mTPQ states.

Once all expectation values of $\langle \hat{h}^n \rangle_k$ ($n = 1, 2, 3$) for the mTPQ states are obtained, it is straightforward to evaluate specific heat and entropy at a temperature $T = 1/(k_B\beta)$ using the cTPQ state $|\beta, N\rangle$ which is defined by

$$|\beta, N\rangle = \exp[-\beta\mathcal{H}/2]|\psi_0\rangle. \quad (9)$$

In the cTPQ method an equilibrium value of \hat{A} at T is

$$\langle \hat{A} \rangle_T = \frac{[\langle \beta, N | \hat{A} | \beta, N \rangle]_{\text{av}}}{[\langle \beta, N | \beta, N \rangle]_{\text{av}}}, \quad (10)$$

where $[\dots]_{\text{av}}$ stands for the arithmetic mean over the initial states $|\psi_0\rangle$ [49]. Specific heat and entropy per pseudospin at T are expressed as

$$C(T) = \frac{N}{T^2} [\langle \hat{h}^2 \rangle_T - (\langle \hat{h} \rangle_T)^2] \quad (11)$$

and

$$S(T) = \frac{\langle \hat{h} \rangle_T}{T} + \frac{1}{N} \ln [\langle \beta, N | \beta, N \rangle]_{\text{av}} + \ln 2, \quad (12)$$

respectively. These $C(T)$ and $S(T)$ can be calculated using

$$\langle \beta, N | \hat{h}^n | \beta, N \rangle = e^{-N\beta\ell} \sum_{k=0}^{\infty} \frac{(N\beta)^{2k}}{(2k)!} Q_k \times \left[\langle \hat{h}^n \rangle_k + \frac{N\beta}{2k+1} (\ell \langle \hat{h}^n \rangle_k - \langle \hat{h}^{n+1} \rangle_k) \right], \quad (13)$$

where $n = 0, 1$, and 2 .

Simulations using the TPQ states were carried out using the simplified Hamiltonian $\mathcal{H} = \mathcal{H}_0 + \mathcal{H}_{3s}$ [Eqs. (1) and (3)]. They were performed on a periodic cluster with $N = 4L^3 = 32$ sites ($L' = 2$), which is illustrated in Fig. 4(a), where L' stands for a linear dimension parallel to the fcc translation vector $(\frac{1}{2}, \frac{1}{2}, 0)$. We note that this $2 \times 2 \times 2$ lattice is the minimal cluster size, by which one can study whether a peak in pseudospin correlations is $\mathbf{k} \sim (\frac{1}{2}, \frac{1}{2}, \frac{1}{2})$ or $(0,0,0)$.

To examine limitations of the TPQ methods especially due to finite-size effects we compare the 32-site simulation using the TPQ states with the large-scale quantum MC (QMC) simulation on a cluster of $N = 4L^3 = 6912$ sites ($L' = 12$) [38], which were performed for the Hamiltonian \mathcal{H}_0 in the negative δ direction ($\delta < 0, q = 0$) (Fig. 1). We performed 32-site simulations with two parameter sets corresponding to the points 1 and 2 in Fig. 1, where QMC data are available [38].

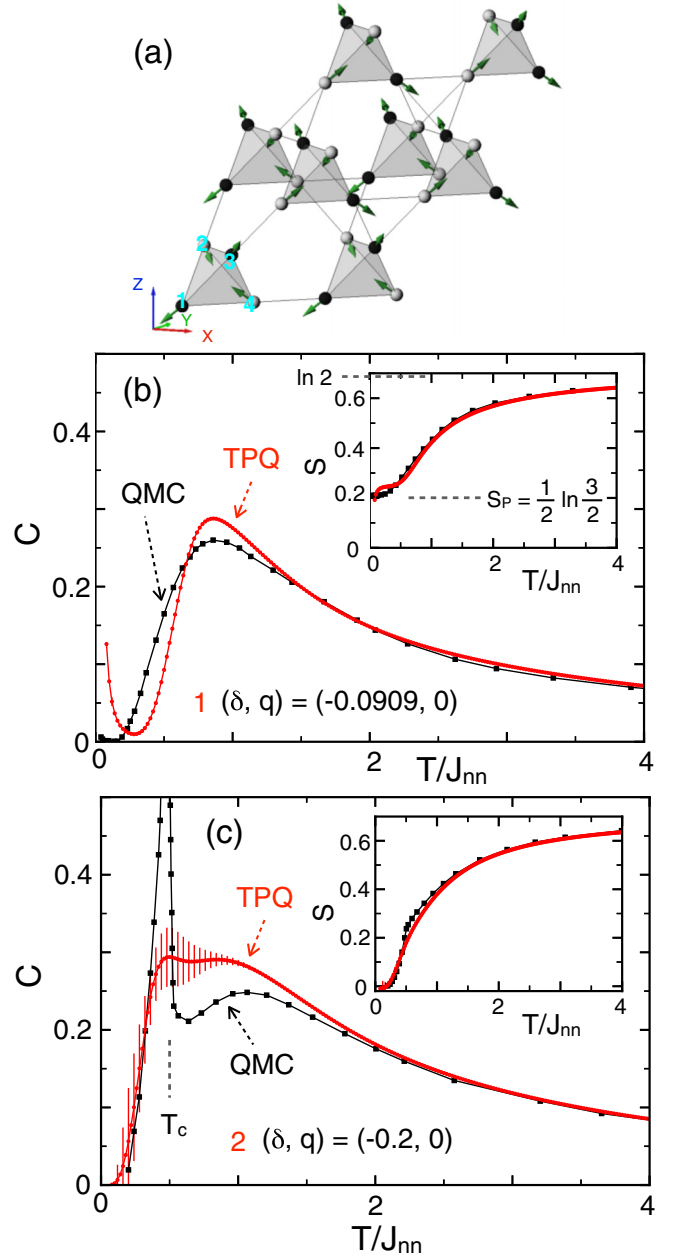


FIG. 4. (a) Periodic 32-site cluster for the simulation using the TPQ states. (b), (c) Specific heat and entropy as a function of temperature obtained by 6912-site QMC (black curve) [38] and the 32-site simulations using the TPQ states without three-spin interaction (red curve) are shown in (b) for the parameters $(\delta, q) = (-0.0909, 0)$ (the point 1 in Fig. 1) and in (c) for $(\delta, q) = (-0.2, 0)$ (the point 2 in Fig. 1), which correspond to the QSI and quadrupole LRO ground states, respectively.

At the point 1 in Fig. 1, $(\delta, q) = (-0.0909, 0)$, δ is larger than the critical value $\delta_c = -0.104$, and the system is in the QSI state at $T = 0$. Specific heat and entropy as a function of temperature are shown in Fig. 4(b). In a high-temperature range of $T/J_{nn} > 0.2$, specific heat and entropy show similar behavior of the classical SI for both simulations. On the other hand, in a lower- T range of $T/J_{nn} < 0.2$ the TPQ result of $C(T)$ shows considerable upturn, which is very different

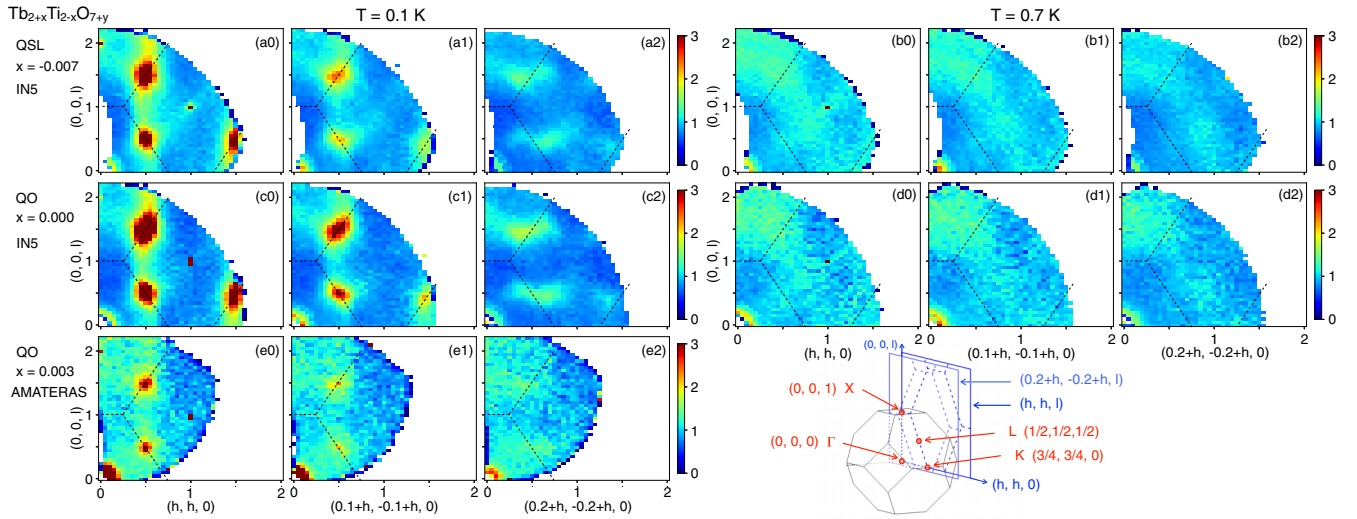


FIG. 5. (a), (b) Intensity maps of 3D data $S(\mathbf{Q})$ of the QSL sample with $x = -0.007$, which were measured on IN5 at 0.1 and 0.7 K, are shown in (a) and (b), respectively. (c), (d) Intensity maps of 3D data $S(\mathbf{Q})$ of the QO sample with $x = 0.000$, which were measured on IN5 at 0.1 and 0.7 K, are shown in (c) and (d), respectively. (e) Intensity maps of 3D data $S(\mathbf{Q})$ of the QO sample with $x = 0.003$, which were measured on AMATERAS at 0.1 K. The 3D data are viewed by 2D slices, which are parallel cross sections of $\mathbf{Q} = (k + h, -k + h, l)$ with fixed $k = 0, 0.1, \text{ and } 0.2$, are shown in (w0), (w1), and (w2) [w=a–e], respectively. Dashed lines in the 2D slices (a)–(e) are boundaries of Brillouin zones. The bottom right corner shows the first Brillouin zone of the fcc lattice (thin black lines), and two 2D slice planes with $k = 0$ and 0.2 (blue lines).

from the QMC result. This is probably a small-size artifact, which is commonly seen in TPQ results at low temperatures [49,51,68].

At the point 2 in Fig. 1, $(\delta, q) = (-0.2, 0)$, δ is smaller than the critical value, and the system is in a quadrupole LRO state at $T = 0$. Specific heat and entropy as a function of temperature are plotted in Fig. 4(c). One can see from this figure that the specific-heat peak at the phase transition temperature $T_c/J_{\text{nn}} \simeq 0.5$ is only slightly seen for the TPQ result, which is the well-known finite-size effect, and that statistical errors of the TPQ result become very large at low temperatures ($T/J_{\text{nn}} < 1$). The large errors at low temperatures are commonly seen in other TPQ results [46,52,54].

From the two comparisons shown in Fig. 4, we can infer that despite the small system size TPQ results can provide useful information on low- T states which have high entropy down to about $T/J_{\text{nn}} = 0.2$ (for the present case). This is in agreement with the studies of the frustrated Heisenberg antiferromagnet on the kagome lattice [49,51]. While we have to cautiously interpret TPQ results, when ground states have classical LROs and finite-temperature phase transitions occur.

IV. RESULTS

A. $S(\mathbf{Q})$ observed by neutron scattering experiments

In the simulations using CMC and the TPQ states equal-time spin correlations are calculated. These correspond to the structure factor $S(\mathbf{Q}) = \int S(\mathbf{Q}, E) dE$. To compare results of the simulations with the previous neutron scattering data [26,34], we integrated $S(\mathbf{Q}, E)$ in an energy range $-0.3 < E < 0.5$ meV, which covers most of the energy spread around $E = 0$ and excludes CF excitations. We constructed 3D data sets of $S(\mathbf{Q}) = \int_{-0.3}^{0.5} S(\mathbf{Q}, E) dE$ which are normalized using the same methods as those described in Refs. [26,34].

Consequently, intensities of $S(\mathbf{Q})$ (arb. units) can be compared mutually among the three samples of TTO.

In Fig. 5 we show intensity maps of the observed $S(\mathbf{Q})$ of the QSL sample with $x = -0.007$ and of the two QO samples with $x = 0.000$ and 0.003 . It is obvious that the pronounced peaks in $S(\mathbf{Q})$ at $\mathbf{k} \sim (\frac{1}{2}, \frac{1}{2}, \frac{1}{2})$ appear only at 0.1 K. An interesting point of these data, which is not seen in the $[S(\mathbf{Q})]_{\text{el}}$ (nominally elastic scattering) data of Ref. [34], is that there are pinch-point-like structures in the $S(\mathbf{Q})$ data at 0.1 K for the QSL sample around $\mathbf{Q} = (0, 0, 2)$ and $(1, 1, 1)$, and that they become weak for the QO samples. This fact is consistent with the interpretation that the QSL sample is located closer to the SI phase (Fig. 1) than the QO samples [27]. It should be noted that the pinch-point-like structures in $S(\mathbf{Q})$ are inelastic scattering.

B. Classical MC simulations

Classical simulations based on the MC method using the Hamiltonian $\mathcal{H}_0 + \mathcal{H}_d + \mathcal{H}_{3s}$ were carried out. By these CMC simulations we can search for candidate parameter sets for TTO in a wider parameter space than the TPQ methods. A guideline of this search is that the spin correlations of TTO are most enhanced in the QO sample with $x = 0.000$ [Fig. 5(c0)], where the quadrupole order is probably small. Assuming small quadrupole LRO (σ_r^+), it is expected that an effective bilinear magnetic coupling term

$$\sum_{i=1}^3 J_{3s,i} \sum_{\langle r, r', r'' \rangle} [e^{i\phi_{r,r''}} \langle \sigma_r^+ \rangle \sigma_r^z \sigma_{r''}^z + \text{H.c.}] \quad (14)$$

becomes at work to lift the SI degeneracy due to $\mathcal{H}_0 + \mathcal{H}_d$, and consequently spin correlations with different wave-vector dependence appear at low temperatures. Therefore, there is

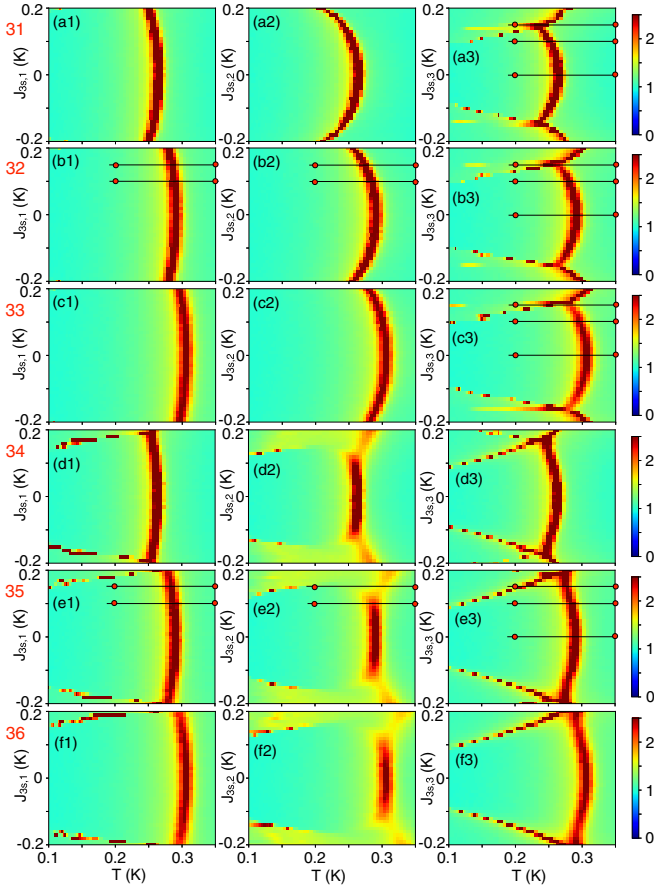


FIG. 6. (a)–(f) Specific heat $C(T, J_{3s,i})$ ($i = 1, 2, 3$; $J_{3s,j \neq i} = 0$) calculated by the 1024-site CMC simulations are shown as color maps: (w1) $C(T, J_{3s,1})$, (w2) $C(T, J_{3s,2})$, and (w3) $C(T, J_{3s,3})$, where $w=a-f$. The parameters (δ, q) of (a)–(f) are $\frac{J_{nn}}{J_{nn}+D_{nn}}(\delta, q) = (-0.1, 0.6)$, $(0.0, 0.55)$, $(0.1, 0.5)$, $(-0.1, -0.6)$, $(0.0, -0.55)$, and $(0.1, -0.5)$, respectively, which correspond to the points 31–36 in Fig. 3.

a chance to find candidate coupling constants $J_{3s,i}$, if the parameters (δ, q) are close to the boundaries of the SI and 3D-PAF phases (Fig. 3), in particular, on the 3D-PAF phase sides.

1. Specific heat in 3D-PAF phases

A number of CMC simulations with a system size $L = 4$ (1024 sites) were performed to study effects of each three-spin interaction on the 3D-PAF phase sides of neighborhoods of the SI and 3D-PAF phase boundaries. The parameters (δ, q) were fixed to the six selected sets: $\frac{J_{nn}}{J_{nn}+D_{nn}}(\delta, q) = (-0.1, 0.6)$, $(0.0, 0.55)$, $(0.1, 0.5)$, $(-0.1, -0.6)$, $(0.0, -0.55)$, and $(0.1, -0.5)$. These correspond to the points 31–36 in Fig. 3, which are in the proposed parameter ranges for the QO sample [27]. The CMC simulations were carried out with many three-spin coupling constants $J_{3s,i}$ in a range $|J_{3s,i}| < 0.2$ K, where one $J_{3s,i} \neq 0$ is finite and the other two $J_{3s,j \neq i} = 0$. Resulting specific-heat data are plotted in Fig. 6 as color maps of $C(T, J_{3s,i})$.

The temperature dependence of specific heat with $J_{3s,i} = 0$, $C(T, J_{3s,i} = 0)$ [Figs. 6(a–f)], is consistent with our previous

CMC simulation study [29], where a single first-order phase transition occurs from the paramagnetic to 3D-PAF states. For finite $J_{3s,i} \neq 0$ another phase transition at a lower temperature occurs, which is noticeably seen in Figs. 6(a3–f3). The lower critical temperature is a phase transition to a state with both quadrupole and magnetic LROs, as will be discussed later. We note that the invariance of the Hamiltonian due to the transformation, $\sigma_r^+ \rightarrow -\sigma_r^+$ and $J_{3s,i} \rightarrow -J_{3s,i}$, is seen in Figs. 6(a–f) as $C(T, J_{3s,i}) \simeq C(T, -J_{3s,i})$. We also note that the symmetry between positive- q and negative- q states for $J_{3s,i} = 0$ does not hold for $J_{3s,i} \neq 0$, which is seen in Figs. 6(a–f) as, e.g., a fact that Fig. 6(a1) ($q = 0.6$) is different from Fig. 6(d1) ($q = -0.6$). Intriguingly, this implies that it is possible to distinguish the 3D-PAF ($q > 0$) order from the 3D-PAF ($q < 0$) order even though the quadrupole order is experimentally invisible, if the three-spin interaction term is finite.

2. Specific heat in SI phase

To study effects of each three-spin interaction on the SI phase sides of neighborhoods of the SI and 3D-PAF phase boundaries, a number of 1024-site CMC simulations were performed with the six selected parameter sets of (δ, q) : $\frac{J_{nn}}{J_{nn}+D_{nn}}(\delta, q) = (-0.1, 0.5)$, $(0.0, 0.45)$, $(0.1, 0.4)$, $(-0.1, -0.5)$, $(0.0, -0.45)$, and $(0.1, -0.4)$. These correspond to the points 37–42 in Fig. 3. The CMC simulations were carried out with many three-spin coupling constants $J_{3s,i}$ in a range $|J_{3s,i}| < 0.2$ K, where one $J_{3s,i} \neq 0$ is finite and the other two $J_{3s,j \neq i} = 0$. Resulting specific-heat data are plotted in Fig. 7 as color maps of $C(T, J_{3s,i})$.

Figures 7(a–f) show that in each simulation there is a single broad peak in the temperature dependence of $C(T, J_{3s,i})$ at $T \sim 0.3$ K, which is the characteristic of the SI model, and that no phase transition appears. These imply that the mechanism expressed by Eq. (14) is much less clear, if the quadrupole moments remain SRO. It seems that long-lived fluctuations of quadrupole moments σ_r^+ do not well function in the mechanism compared to the average $\langle \sigma_r^+ \rangle$ within the CMC simulations.

3. $S(Q)$ in 3D-PAF phases ($\delta = 0$)

Classical MC simulations were carried out with a larger system size $L = 10$ (16 000 sites) to study effects of each three-spin interaction on the structure factor $S(Q)$. We calculated $S(Q)$ in the 3D-PAF phases. Considering the results of Sec. IV B 1, the parameters (δ, q) were fixed to the two sets: $\frac{J_{nn}}{J_{nn}+D_{nn}}(\delta, q) = (0.0, 0.55)$ and $(0.0, -0.55)$, corresponding to the points 32 and 35 in Fig. 3. The three-spin interaction constant was fixed to two typical values: $J_{3s,i} = 0.1$ and 0.15 K ($J_{3s,j \neq i} = 0$). Figure 8 shows the resulting intensity maps of $S(Q)$ which are calculated with the parameters corresponding to the red circles in Figs. 6(b1–b3), and at two temperatures 0.2 and 0.35 K, below and above the phase transition temperature of the 3D-PAF ($q > 0$) LRO. Figure 9 shows the resulting intensity maps of $S(Q)$ which are calculated with the parameters corresponding to the red circles in Figs. 6(e1–e3), and at 0.2 and 0.35 K, below and above the phase transition temperature of the 3D-PAF ($q < 0$) LRO.

When the three-spin interactions are set to zero, the calculated $S(Q)$ with $\frac{J_{nn}}{J_{nn}+D_{nn}}q = 0.55$ and -0.55 , which are

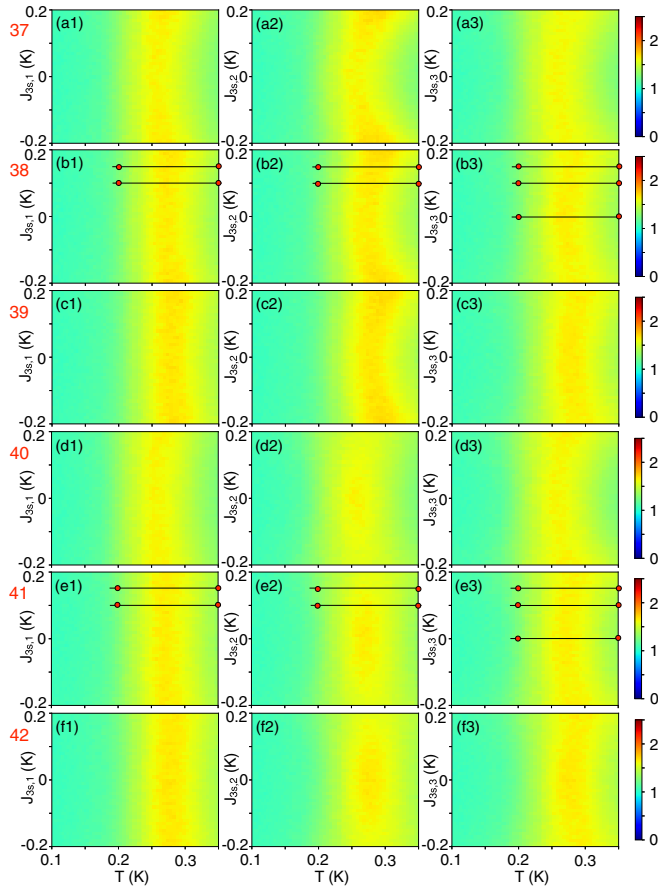


FIG. 7. (a)–(f) Specific heat $C(T, J_{3s,i})$ ($i = 1, 2, 3$; $J_{3s,j \neq i} = 0$) calculated by the 1024-site CMC simulation are shown as color maps: (w1) $C(T, J_{3s,1})$, (w2) $C(T, J_{3s,2})$, and (w3) $C(T, J_{3s,3})$, where $w=a-f$. The parameters (δ, q) of (a)–(f) are $\frac{J_{3s,3}}{J_{nn}+D_{nn}}(\delta, q) = (-0.1, 0.5)$, $(0.0, 0.45)$, $(0.1, 0.4)$, $(-0.1, -0.5)$, $(0.0, -0.45)$, and $(0.1, -0.4)$, respectively, which correspond to the points 37–42 in Fig. 3.

Figs. 8(m,n) and Figs. 9(m,n), respectively, show almost the same characteristics: the pinch-point structure of the SI is seen around the Γ points $(0,0,2)$ and $(1,1,1)$, the intensity pattern becomes weakened owing to the quadrupole order as temperature is lowered below T_c , the intensity pattern is scarcely affected by the quadrupole structures ($q > 0$ or $q < 0$).

When the three-spin interactions are switched on, $S(\mathbf{Q})$ at 0.35 K [Figs. 8(b,d,f,h,j,l) and 9(b,d,f,h,j,l)] show little dependence on $J_{3s,i}$, while $S(\mathbf{Q})$ at 0.2 K [Figs. 8(a,c,e,g,i,k) and 9(a,c,e,g,i,k)] show large changes depending on the value of $J_{3s,i}$. In particular, for $J_{3s,3} = 0.15$ K magnetic Bragg peaks appear at 0.2 K [Figs. 8(i0) and 9(i0)]. This is consistent with the interpretation that the second phase transitions [Figs. 6(b3,e3)] are ascribed to magnetic ordering in addition to the 3D-PAF LRO. We will not delve into these magnetic phase transitions, order parameters, etc., in this study. The magnetic LRO of the pyrochlore magnet $\text{Tb}_2\text{Sn}_2\text{O}_7$ [69] may possibly be accounted for by the three-spin interaction term.

The most interesting results of the calculated $S(\mathbf{Q})$ are those for $J_{3s,3} = 0.1$ K and $q > 0$ [Figs. 8(k,l)]. It is obvious that the calculated $S(\mathbf{Q})$ at 0.2 K [Fig. 8(k0)] bears a resemblance to the observed $S(\mathbf{Q})$ of TTO at 0.1 K

[Figs. 5(a0,c0,e0)], in a sense that they commonly show peaks at $\mathbf{Q} = (\frac{1}{2}, \frac{1}{2}, \frac{1}{2})$ and $(\frac{1}{2}, \frac{1}{2}, \frac{3}{2})$. In addition, the temperature dependence of the calculated $S(\mathbf{Q})$ shows that the intensity pattern changes from the peaked structure around $\mathbf{Q} = (\frac{1}{2}, \frac{1}{2}, \frac{1}{2})$ at 0.2 K to a pinch-point-like pattern of the classical SI at 0.35 K [Figs. 8(k,l)]. This roughly agrees with the temperature variation of the observed $S(\mathbf{Q})$ of TTO [Figs. 5(a–d)]. In contrast, for $J_{3s,3} = 0.1$ K and $q < 0$ the calculated $S(\mathbf{Q})$ at 0.2 K [Fig. 9(k0)] shows a very different intensity pattern from $S(\mathbf{Q})$ shown in Fig. 8(k0). This can be understood by the difference in the quadrupole orders [Figs. 1(b,c)] and in the effective bilinear interactions [Eq. (14)]. Thus, we can conclude that the CMC simulation results suggest that a parameter set that should be further investigated, especially using techniques for many-body quantum states, is $\frac{J_{3s,3}}{J_{nn}+D_{nn}}(\delta, q) \sim (0.0, 0.55)$, $J_{3s,1} = J_{3s,2} = 0$, and $\frac{J_{3s,3}}{J_{nn}+D_{nn}} \sim 0.1$ (or -0.1). We also conclude that the $q < 0$ sides of the phase diagrams (Figs. 1 and 3) can be excluded from studies of TTO.

It should be noted that the interesting results [Figs. 8(k, l)] are obtained for the parameters of the Hamiltonian, which are close to the classical phase boundaries [Fig. 6(b3)]. Theoretically, effects of proximity to phase boundaries separating two or three LROs in the pyrochlore magnets were studied in Refs. [43,70] based on the generic bilinear NN Hamiltonian. It was shown that a disordered ground state can be induced by nontrivial degeneracy of the order parameters around the phase boundary. This mechanism may be related to that of the disordered ground state of TTO.

4. Other results of $S(\mathbf{Q})$

To complement $S(\mathbf{Q})$ shown in Sec. IV B 3 (Figs. 8 and 9) we performed several 16 000-site CMC simulations with parameters $\frac{J_{3s,3}}{J_{nn}+D_{nn}}(\delta, q) = (-0.1, 0.6)$, $(0.1, 0.5)$, $(0.0, 0.45)$, and $(0.0, -0.45)$ corresponding to the points 31, 33, 38, and 41 in Fig. 3, respectively. These results are presented in Appendices C and D.

C. Quantum simulations using TPQ states

Quantum simulations using the TPQ states were carried out to confirm the classical MC results shown in Figs. 8(k0), 16(c0), and 17(c0). There were two practical problems. First, since the computation was very time consuming, the number of the simulations was limited to far less than that of the CMC simulations. Second, since it was memory-intensive task, the system size was limited to only 32 sites, which precluded us from studying systematic size dependence. Thus, we had to carefully interpret results of the simulations by paying particular attention to changes of results with varying interaction parameters. For example, by comparing results with $J_{3s,3} = 0$ and $J_{3s,3} \neq 0$ it was not difficult to discern effects of $J_{3s,3}$ from those due to the small size. Based on this idea, many 32-site simulations using the TPQ states were carried out using the Hamiltonian $\mathcal{H}_0 + \mathcal{H}_{3s}$ with $J_{3s,3}/J_{nn} = 0.1$ and 0, where $J_{3s,1} = J_{3s,2} = 0$ were fixed to zero. The parameters (δ, q) were systematically changed mainly on the q axis ($\delta = 0$) in Fig. 1, where (δ, q) values we selected are indicated by the red circles, the points 3–29.

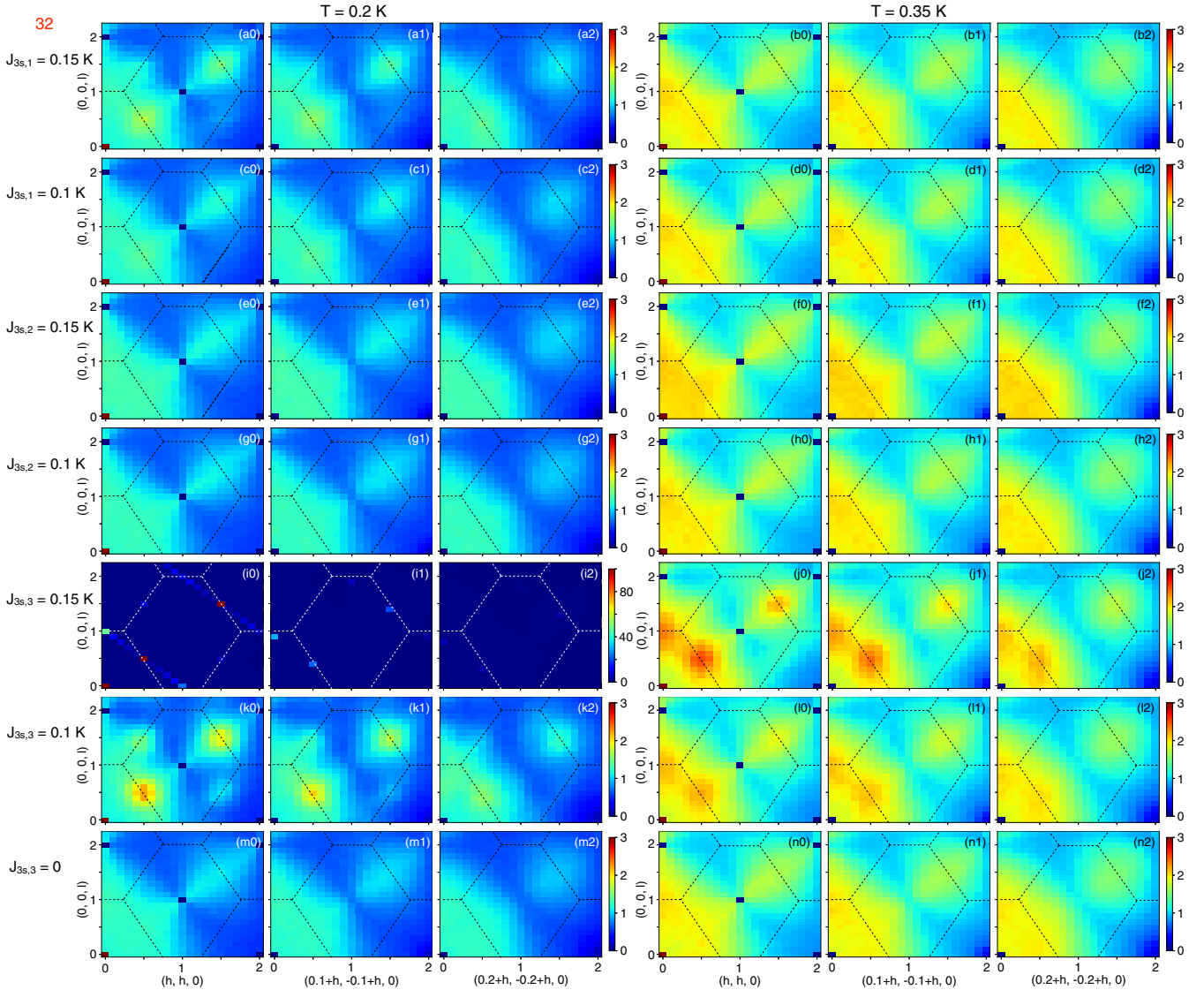


FIG. 8. Intensity maps of $S(\mathbf{Q})$ calculated by the 16 000-site CMC simulations using parameters indicated by red circles shown in Figs. 6(b1–b3) ($J_{3s,i}$; $i = 1, 2, 3$; $J_{3s,j \neq i} = 0$) and by the point 32 in Fig. 3 [$\frac{J_{nn}}{J_{nn}+D_{nn}}(\delta, q) = (0.0, 0.55)$]. They are viewed by 2D slices of $\mathbf{Q} = (k+h, -k+h, l)$ with fixed $k = 0, 0.1$, and 0.2 , which are shown in (w0), (w1), and (w2) [$w = a-n$], respectively. They are calculated at two temperatures 0.2 K (a,c,e,g,i,k,m) and 0.35 K (b,d,f,h,j,l,n), below and above the phase transition temperature of the 3D-PAF ($q > 0$) LRO. Intensity maps for $J_{3s,1} = 0.15$ and 0.1 K [Fig. 6(b1)] are shown in (a,b) and (c,d), respectively. Intensity maps for $J_{3s,2} = 0.15$ and 0.1 K [Fig. 6(b2)] are shown in (e,f) and (g,h), respectively. Intensity maps for $J_{3s,3} = 0.15, 0.1$, and 0 K [Fig. 6(b3)] are shown in (i,j), (k,l), and (m,n), respectively.

1. Specific heat and entropy on q axis

Several 32-site simulations using the cTPQ state with the parameters $(\delta = 0, q)$ on the q axis were carried out for $J_{3s,3}/J_{nn} = 0$ and 0.1 ($J_{3s,1} = J_{3s,2} = 0$). Resulting temperature dependence of specific heat $C(T)$ and entropy $S(T)$ are plotted in Figs. 10 and 11. For $J_{3s,3} = 0$, $C(T)$ and $S(T)$ curves with positive q values [Figs. 10(a,c)] are almost the same as corresponding curves with negative q [Figs. 10(b,d)]. This fact [$C(T, q) = C(T, -q)$, $S(T, q) = S(T, -q)$] reflects the invariance of the Hamiltonian \mathcal{H}_0 under the transformation of rotating σ_r about the local z_r axis by $\pi/2$ and $q \rightarrow -q$. For $J_{3s,3} \neq 0$ this invariance does not hold, resulting in $C(T, q) \neq C(T, -q)$ [Figs. 11(a,b)] and $S(T, q) \neq S(T, -q)$ [Figs. 11(c,d)].

For $J_{3s,3}/J_{nn} = 0$, each curve of $C(T)$ and $S(T)$ (Fig. 10) with q in a range $0 \leq |q| \leq 0.45$ has a single broad peak [Figs. 10(a,b)] and an entropy plateau ($S \simeq 0.25$) [Figs. 10(c,d)], respectively. These behaviors are the characteristics of the classical SI [Fig. 4(b)], which are expected also for QSI at intermediate temperatures [38]. The discrepancy of the value of the entropy plateau $S \simeq 0.25$ from the the Pauling entropy $S = \frac{1}{2} \ln \frac{3}{2}$ may be caused by a small size effect. Each curve of $C(T)$ and $S(T)$ (Fig. 10) with q in a range $|q| \geq 0.5$ has a low- T peak and the zero- T limit $S(T \rightarrow 0) \simeq 0$, respectively. The low- T peak of $C(T)$, which is similar to that of Fig. 4(c), implies that a phase transition to a quadrupole-ordered state occurs. These results shown in Fig. 10 for $J_{3s,3}/J_{nn} = 0$ suggest that the quantum phase

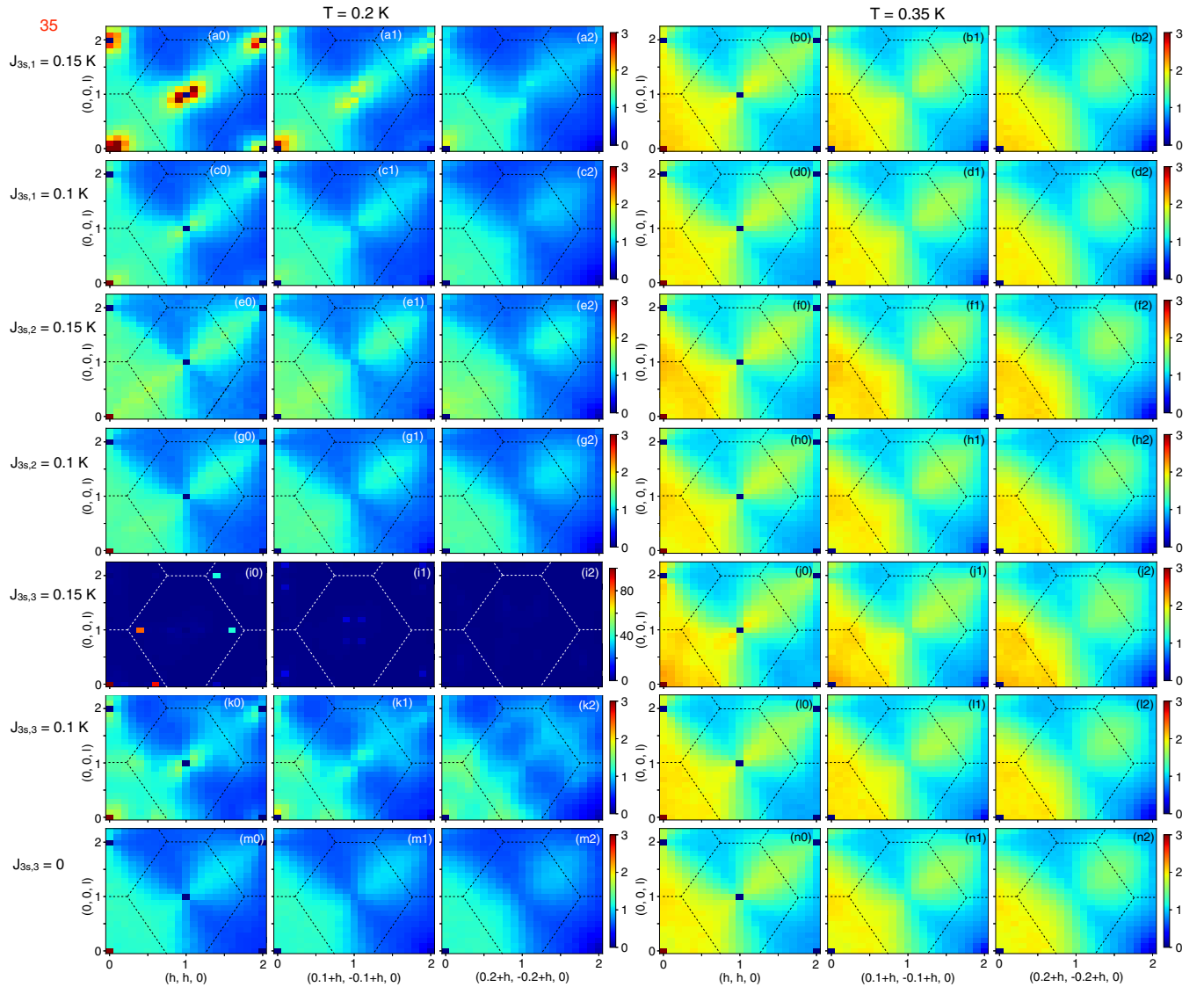


FIG. 9. Intensity maps of $S(\mathbf{Q})$ calculated by the 16 000-site CMC simulations using parameters indicated by red circles shown in Figs. 6(e1–e3) ($J_{3s,i}$; $i = 1, 2, 3$; $J_{3s,j \neq i} = 0$) and by the point 35 in Fig. 3 [$\frac{J_{nn}}{J_{nn}+D_{nn}}(\delta, q) = (0.0, -0.55)$]. They are viewed by 2D slices of $\mathbf{Q} = (k + h, -k + h, l)$ with fixed $k = 0, 0.1, \text{ and } 0.2$, which are shown in (w0), (w1), and (w2) [$w = a-n$], respectively. They are calculated at two temperatures 0.2 K (a,c,e,g,i,k,m) and 0.35 K (b,d,f,h,j,l,n), below and above the phase transition temperature of the 3D-PAF ($q < 0$) LRO. Intensity maps for $J_{3s,1} = 0.15$ and 0.1 K [Fig. 6(e1)] are shown in (a,b) and (c,d), respectively. Intensity maps for $J_{3s,2} = 0.15$ and 0.1 K [Fig. 6(e2)] are shown in (e,f) and (g,h), respectively. Intensity maps for $J_{3s,3} = 0.15, 0.1, \text{ and } 0$ K [Fig. 6(e3)] are shown in (i,j), (k,l), and (m,n), respectively.

boundaries on the q axis are not very different from the classical phase boundaries $|q_c| = \frac{1}{2}$ ($\delta = 0$, Fig. 1).

For $J_{3s,3}/J_{nn} = 0.1$, each curve of $C(T)$ and $S(T)$ (Fig. 11) with q in a range $-0.4 \leq q \leq 0.45$ has a single broad peak [Figs. 11(a,b)] and the entropy plateau ($S \simeq 0.25$) [Figs. 11(c,d)], respectively. These can be understood by the classical SI behaviors expected for QSI at intermediate temperatures. The upturn of $C(T)$ [Figs. 11(a,b)] and the downturn of $S(T)$ [Figs. 11(c,d)] in a low- T range of $T/J_{nn} < 0.2$ suggest certain QSL behavior [38] or/and an artifact caused by the small size [Fig. 4(b)]. It seems difficult to correctly draw information from low- T data in $T/J_{nn} < 0.2$. This sort of difficulty due to the small system size has been ob-

served in studies of the frustrated Heisenberg antiferromagnet on the kagome lattice at low temperatures [49,51,68].

For $J_{3s,3}/J_{nn} = 0.1$, each curve of $C(T)$ and $S(T)$ (Fig. 11) with q in ranges $q \geq 0.6$ and $q \leq -0.55$ has a low- T peak and the zero- T limit $S(T \rightarrow 0) \simeq 0$, respectively. The low- T peak of $C(T)$ [Figs. 11(a,b)], which is similar to that of Fig. 4(c), implies that a phase transition to a quadrupole-ordered state occurs. The low- T peaks of $C(T)$ with $q = -0.45, -0.5$ [Fig. 11(b)] could also be understood by T_c of the quadrupole LRO, although these are less clear. On the other hand, the low- T behavior of $C(T)$ with $q = 0.5, 0.55$ [Fig. 11(a)] suggests that something different happens at low temperatures. These $C(T)$ curves show roughly the behavior of $C(T) \sim \text{const}$ in

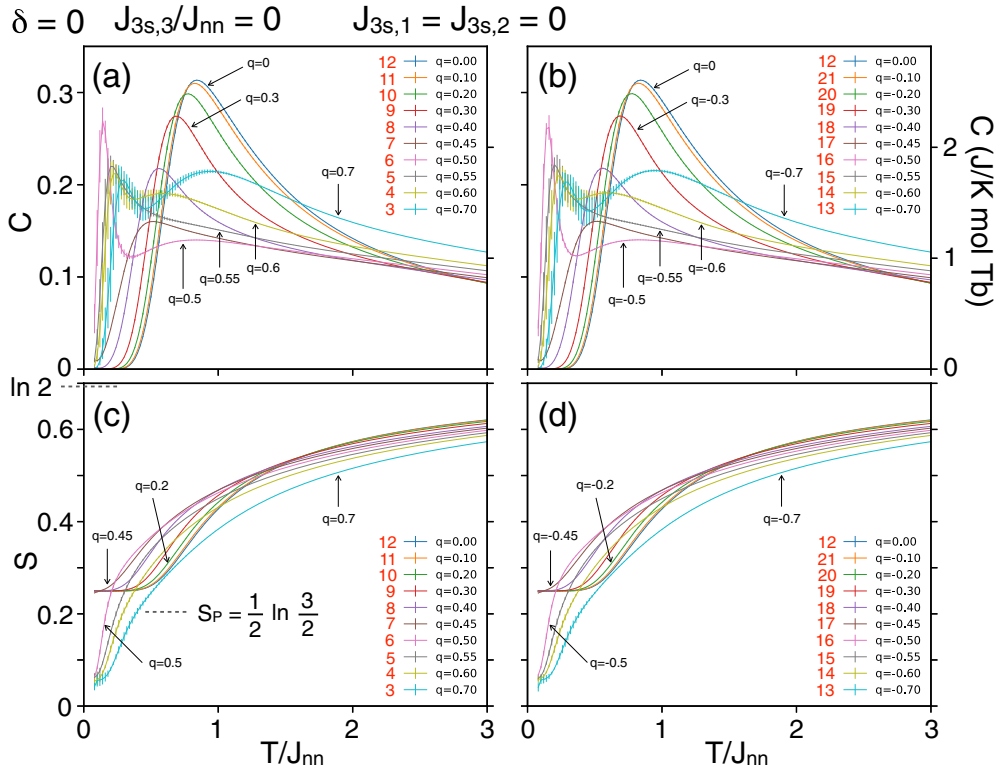


FIG. 10. Temperature dependence of specific heat $C(T)$ and entropy $S(T)$ obtained by the 32-site simulations using the cTPQ state for $J_{3s,3}/J_{nn} = 0$ ($J_{3s,1} = J_{3s,2} = 0$) with parameters ($\delta = 0, q$), the points 3–21 in Fig. 1. In (a) and (b) $C(T)$ for $q \geq 0$ and $q \leq 0$ are shown, respectively. In (c) and (d) $S(T)$ for $q \geq 0$ and $q \leq 0$ are shown, respectively.

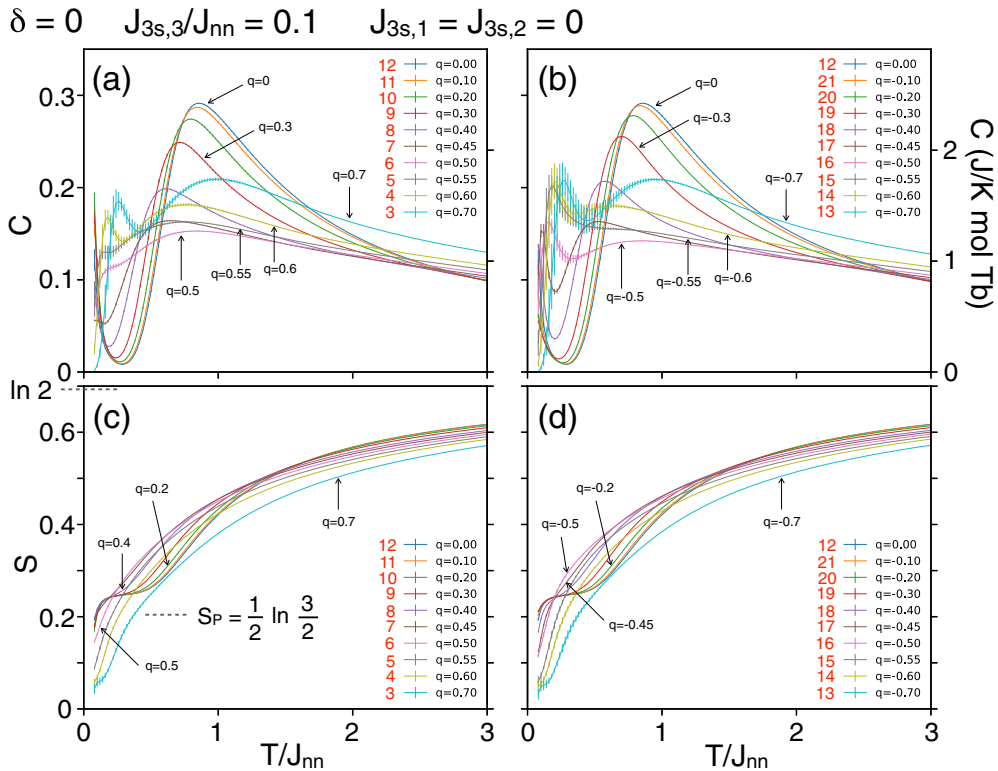


FIG. 11. Temperature dependence of specific heat $C(T)$ and entropy $S(T)$ obtained by the 32-site simulations using the cTPQ state for $J_{3s,3}/J_{nn} = 0.1$ ($J_{3s,1} = J_{3s,2} = 0$) with parameters ($\delta = 0, q$), the points 3–21 in Fig. 1. In (a) and (b) $C(T)$ for $q \geq 0$ and $q \leq 0$ are shown, respectively. In (c) and (d) $S(T)$ for $q \geq 0$ and $q \leq 0$ are shown, respectively.

$T/J_{\text{nn}} < 1$, which is reminiscent of $C(T)$ data of the TTO experiments [24]. Intriguingly, the Hamiltonian with one of these parameters, $q = 0.55$, is one of the candidates for TTO suggested by the CMC simulations [Fig. 8(k0)].

2. $S(\mathbf{Q})$ on q axis ($q \geq 0$)

We calculated $S(\mathbf{Q})$ and the expectation values of pseudospin correlations using the mTPQ method [Eqs. (7) and (8)] to take a closer look at temperature and q dependence of the states. By choosing two typical temperatures $T/J_{\text{nn}} = 1$ and 0.2, which are above and below the specific heat peak (or bump), 2D slice view data of $S(\mathbf{Q})$ and $\langle \sigma_{\mathbf{Q}}^{\alpha} \sigma_{-\mathbf{Q}}^{\alpha} \rangle$ ($\alpha = z, x$) in the plane $\mathbf{Q} = (h, h, l)$ were calculated. These 2D slices with the parameters ($\delta = 0, q \geq 0$), the points 3–12 in Fig. 1, for $J_{3s,3}/J_{\text{nn}} = 0$ and 0.1 ($J_{3s,1} = J_{3s,2} = 0$) are shown in Figs. 12 and 13, respectively.

For $J_{3s,3}/J_{\text{nn}} = 0$ and $(\delta, q) = (0, 0)$, i.e., the classical SI model, $S(\mathbf{Q})$ and $\langle \sigma_{\mathbf{Q}}^{\alpha} \sigma_{-\mathbf{Q}}^{\alpha} \rangle$ ($\alpha = z, x$) are shown in Figs. 12(j1–j6). Since there is no interaction between quadrupole moments, $\langle \sigma_{\mathbf{Q}}^x \sigma_{-\mathbf{Q}}^x \rangle$ [Figs. 12(j3,j6)] do not depend on \mathbf{Q} . Wave-vector dependence of $S(\mathbf{Q})$ [Figs. 12(j1,j4)] and $\langle \sigma_{\mathbf{Q}}^z \sigma_{-\mathbf{Q}}^z \rangle$ [Figs. 12(j2,j5)] show intensity patterns which scarcely appear in simulations of pyrochlore magnets. They probably reflect the periodic 32-site cluster because $\langle \sigma_{\mathbf{Q}}^z \sigma_{-\mathbf{Q}}^z \rangle$ [Figs. 12(j2,j5)] bear a resemblance to Fig. 6 of Ref. [56], in which a DMRG technique on the 32-site cluster was used for the Heisenberg antiferromagnet on the pyrochlore lattice [$(\delta, q) = (1, 0)$]. In addition, owing to the 32-site cluster without the cubic symmetry, $S(\mathbf{Q})$, $\langle \sigma_{\mathbf{Q}}^z \sigma_{-\mathbf{Q}}^z \rangle$, and $\langle \sigma_{\mathbf{Q}}^x \sigma_{-\mathbf{Q}}^x \rangle$ show distinct intensity patterns along the [111] and $[1\bar{1}\bar{1}]$ directions. Therefore, the intensity pattern of $S(\mathbf{Q})$ [Figs. 12(j1,j4)] can be regarded as a 32-site-cluster version of the classical SI. We note that for large clusters the pattern should be characterized by the pinch point [see Fig. 3 of Ref. [38], Fig. 18(n0), etc.].

For $J_{3s,3}/J_{\text{nn}} = 0$ and $(\delta, q) = (0, 0.7)$, where the system has the ground state with the 3D-PAF ($q > 0$) quadrupole order (Fig. 1), $S(\mathbf{Q})$ and $\langle \sigma_{\mathbf{Q}}^{\alpha} \sigma_{-\mathbf{Q}}^{\alpha} \rangle$ ($\alpha = z, x$) are shown in Figs. 12(a1–a6). Bragg-type peaks due to the 3D-PAF ($q > 0$) order are seen in $\langle \sigma_{\mathbf{Q}}^x \sigma_{-\mathbf{Q}}^x \rangle$ [Fig. 12(a3)] at $\mathbf{Q} = (1, 1, 1)$ and $(1, 1, 3)$. While $S(\mathbf{Q})$ [Fig. 12(a1)] and $\langle \sigma_{\mathbf{Q}}^z \sigma_{-\mathbf{Q}}^z \rangle$ [Fig. 12(a2)] at $T/J_{\text{nn}} = 0.2$ show magnetic SRO patterns which resemble those of the classical SI [Figs. 12(j1,j2)], although intensities become weaker.

For $J_{3s,3}/J_{\text{nn}} = 0$ and $(\delta = 0, 0 < q < 0.7)$, $S(\mathbf{Q})$ and $\langle \sigma_{\mathbf{Q}}^{\alpha} \sigma_{-\mathbf{Q}}^{\alpha} \rangle$ ($\alpha = z, x$) [Figs. 12(b–i)] continuously change in the range $0 < q < 0.7$, i.e., from the classical SI to the 3D-PAF ($q > 0$) order. At $T/J_{\text{nn}} = 0.2$ and around $q = 0.5$ [Figs. 12(c1–e1,c2–e2,c3–e3)] they change steeply as a function of q , which is in agreement with the q dependence of $C(T)$ curves [Fig. 10(a)]. This steep change can be ascribed to a first-order phase transition at $T = 0$ in the thermodynamic limit $N \rightarrow \infty$ [31,32].

For $J_{3s,3}/J_{\text{nn}} = 0.1$, at $T/J_{\text{nn}} = 1$ $S(\mathbf{Q})$ [Figs. 13(a4–j4)] and $\langle \sigma_{\mathbf{Q}}^{\alpha} \sigma_{-\mathbf{Q}}^{\alpha} \rangle$ ($\alpha = z, x$) [Figs. 13(a5–j5,a6–j6)] are almost the same as those for $J_{3s,3}/J_{\text{nn}} = 0$ [Figs. 12(a4–j4,a5–j5,a6–j6)]. This means that at this temperature $k_{\text{B}}T$ is much larger than the energy scale of the three-spin interaction. On the other hand, at $T/J_{\text{nn}} = 0.2$ $S(\mathbf{Q})$ [Figs. 13(a1–j1)] and $\langle \sigma_{\mathbf{Q}}^{\alpha} \sigma_{-\mathbf{Q}}^{\alpha} \rangle$ ($\alpha = z, x$) [Figs. 13(a2–j2,a3–j3)] are very different from

those for $J_{3s,3}/J_{\text{nn}} = 0$ [Figs. 12(a1–j1,a2–j2,a3–j3)]. This implies that $k_{\text{B}}T$ becomes comparable to (or lower than) the energy scale of the three-spin interaction.

For $J_{3s,3}/J_{\text{nn}} = 0.1$ and at $T/J_{\text{nn}} = 0.2$, $S(\mathbf{Q})$ with q in a range $0 \leq q \leq 0.4$ [Figs. 13(f1–j1)] show mutually similar intensity patterns, which are very different from those for $J_{3s,3}/J_{\text{nn}} = 0$ [Figs. 12(f1–j1)]. This difference can be brought about by lifting the SI degeneracy due to the three-spin interaction, which is probably small, because $S(T)$ curves ($0 \leq q \leq 0.4$) plotted in Figs. 10(c) and 11(c) show only slight difference between $J_{3s,3}/J_{\text{nn}} = 0.1$ and 0 in $T/J_{\text{nn}} > 0.2$.

For $J_{3s,3}/J_{\text{nn}} = 0.1$ and at $T/J_{\text{nn}} = 0.2$, $S(\mathbf{Q})$ with $q = 0.5, 0.55, 0.6$ [Figs. 13(b1–d1)] show a novel intensity pattern characterized by magnetic spin correlations with $\mathbf{k} \sim (\frac{1}{2}, \frac{1}{2}, \frac{1}{2})$. These spin correlations roughly agree with those of the CMC results [Figs. 8(k0), 16(c0), and 17(c0)]. Therefore, we may conclude that the spin correlations of TTO [Figs. 5(a0,c0,e0)] can be basically accounted for by these TPQ and CMC results, although detailed structures of the intensity patterns are not the same. In other words, the TPQ results suggest that the effective Hamiltonian minimally describing TTO is $\mathcal{H}_0 + \mathcal{H}_{3s}$ with $J_{3s,1} = J_{3s,2} = 0$, $J_{3s,3}/J_{\text{nn}} \sim 0.1$ (or -0.1) and the parameters (δ, q) in the region which is enclosed by the red dashed line in Fig. 1, where $\delta \neq 0$ will be discussed in Appendix E. Another interesting point one can see from Figs. 13(c1–c3,d1–d3) is that $\langle \sigma_{\mathbf{Q}}^x \sigma_{-\mathbf{Q}}^x \rangle$ with $q = 0.5, 0.55$ [Figs. 13(c3,d3)] show broad peaks around Γ points, i.e., electric quadrupole correlations with $\mathbf{k} \sim \mathbf{0}$. These results [Figs. 13(c1–c3,d1–d3)] imply that the magnetic dipole correlations and electric quadrupole correlations coexist at $T/J_{\text{nn}} = 0.2$. This coexistence may possibly continue down to $T = 0$.

3. $S(\mathbf{Q})$ on q axis ($q < 0$)

Two-dimensional slices of $S(\mathbf{Q})$ and $\langle \sigma_{\mathbf{Q}}^{\alpha} \sigma_{-\mathbf{Q}}^{\alpha} \rangle$ ($\alpha = z, x$) calculated with the parameters ($\delta = 0, q < 0$), the points 13–21 in Fig. 1, for $J_{3s,3}/J_{\text{nn}} = 0$ and 0.1 ($J_{3s,1} = J_{3s,2} = 0$) are shown in Figs. 14 and 15, respectively.

For $J_{3s,3}/J_{\text{nn}} = 0$, $S(\mathbf{Q})$ [Figs. 14(a1–i1,a4–i4)] and $\langle \sigma_{\mathbf{Q}}^z \sigma_{-\mathbf{Q}}^z \rangle$ [Figs. 14(a2–i2,a5–i5)] are the same as those with ($\delta = 0, q > 0$) [Figs. 12(a1–i1,a4–i4) and 12(a2–i2,a5–i5)], while $\langle \sigma_{\mathbf{Q}}^x \sigma_{-\mathbf{Q}}^x \rangle$ [Figs. 14(a3–i3,a6–i6)] are different from those with ($\delta = 0, q > 0$) [Figs. 12(a3–i3,a6–i6)]. These are consequences of the invariance of \mathcal{H}_0 under the transformation of rotating σ_r about the local z_r axis by $\pi/2$ and $q \rightarrow -q$, confirming the correctness of the simulations using the TPQ states.

For $J_{3s,3}/J_{\text{nn}} = 0.1$ and at $T/J_{\text{nn}} = 0.2$, $S(\mathbf{Q})$ and $\langle \sigma_{\mathbf{Q}}^z \sigma_{-\mathbf{Q}}^z \rangle$ with $q \leq -0.45$ [Figs. 15(a1–e1,a2–e2)] are different from those with $q \geq 0.45$ [Figs. 13(a1–e1,a2–e2)], which results from breaking of the invariance for $\mathcal{H}_0 + \mathcal{H}_{3s}$. In relation to the analysis of TTO, none of $S(\mathbf{Q})$ [Figs. 15(a1–e1)] show spin correlations with $\mathbf{k} \sim (\frac{1}{2}, \frac{1}{2}, \frac{1}{2})$, which is in agreement with the CMC results with $q < 0$ (Figs. 9 and 19). Therefore, we conclude again that the $q < 0$ side of the phase diagram (Fig. 1) can be excluded from studies of TTO.

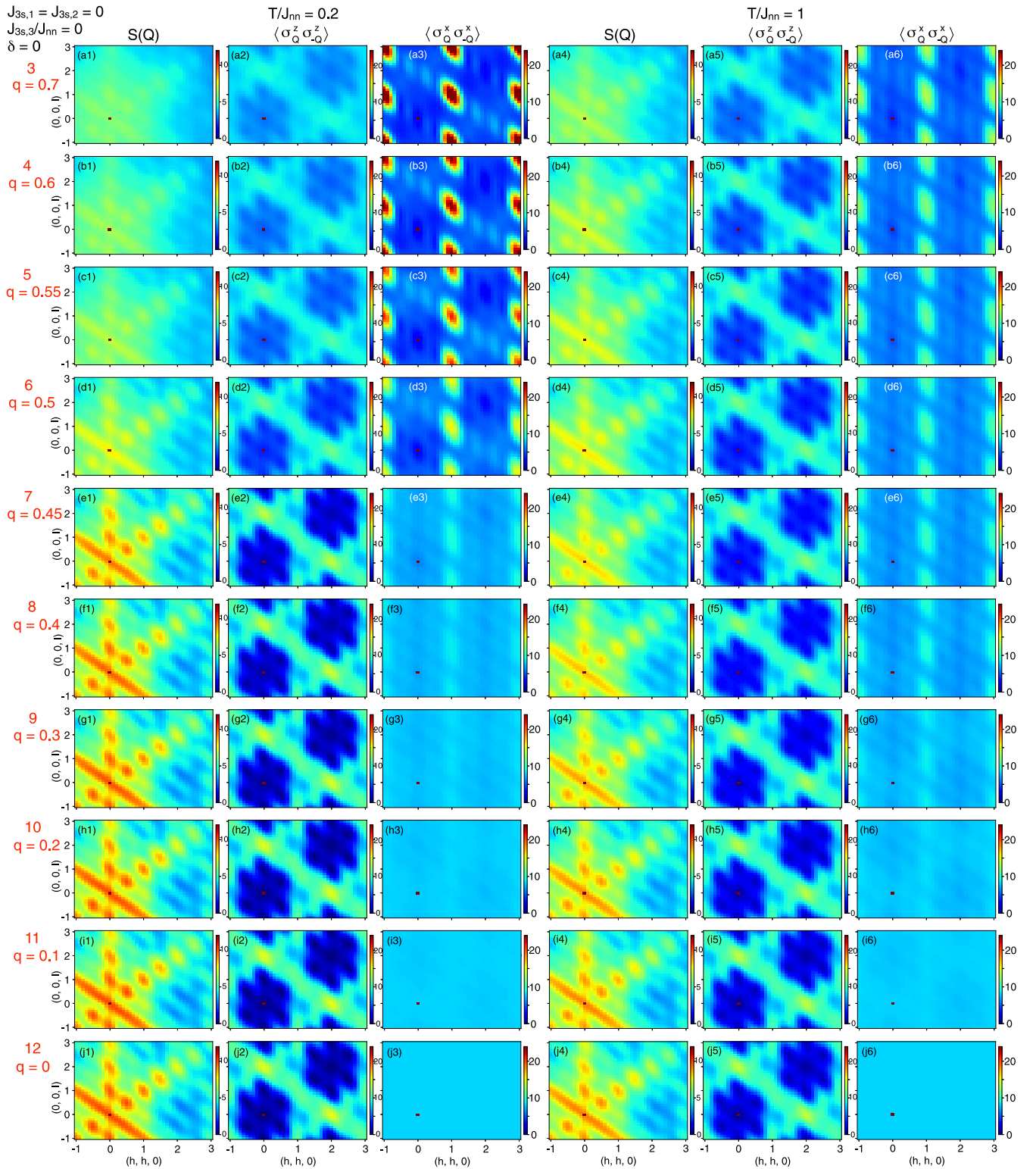


FIG. 12. Two-dimensional slices of (w1,w4) $S(\mathbf{Q})$, (w2,w5) $\langle \sigma_Q^z \sigma_{-Q}^z \rangle$, and (w3,w6) $\langle \sigma_Q^x \sigma_{-Q}^x \rangle$ [$w=a-j$] in the plane $\mathbf{Q} = (h, h, l)$ calculated by the 32-site simulations using the mTPQ state for $J_{3s,3}/J_{nn} = 0$ ($J_{3s,1} = J_{3s,2} = 0$) with parameters ($\delta = 0, q \geq 0$), the points 3–12 in Fig. 1. The 2D slice data at $T/J_{nn} = 0.2$ and 1 are shown in (w1)–(w3) and (w4)–(w6) [$w=a-j$], respectively.

For $J_{3s,3}/J_{nn} = 0$ and ($\delta = 0, -0.7 < q < 0$), $S(\mathbf{Q})$ and $\langle \sigma_Q^\alpha \sigma_{-Q}^\alpha \rangle$ ($\alpha = z, x$) [Figs. 14(b–i)] continuously change in the range $-0.7 < q < 0$, i.e., from the classical SI to the 3D-PAF ($q < 0$) order. At $T/J_{nn} = 0.2$ and around

$q = -0.5$ [Figs. 14(c1–e1,c2–e2,c3–e3)] they change very steeply as a function of q , which is consistent with the q dependence of $C(T)$ [Fig. 10(b)]. This steep change can be ascribed to a first-order phase tran-

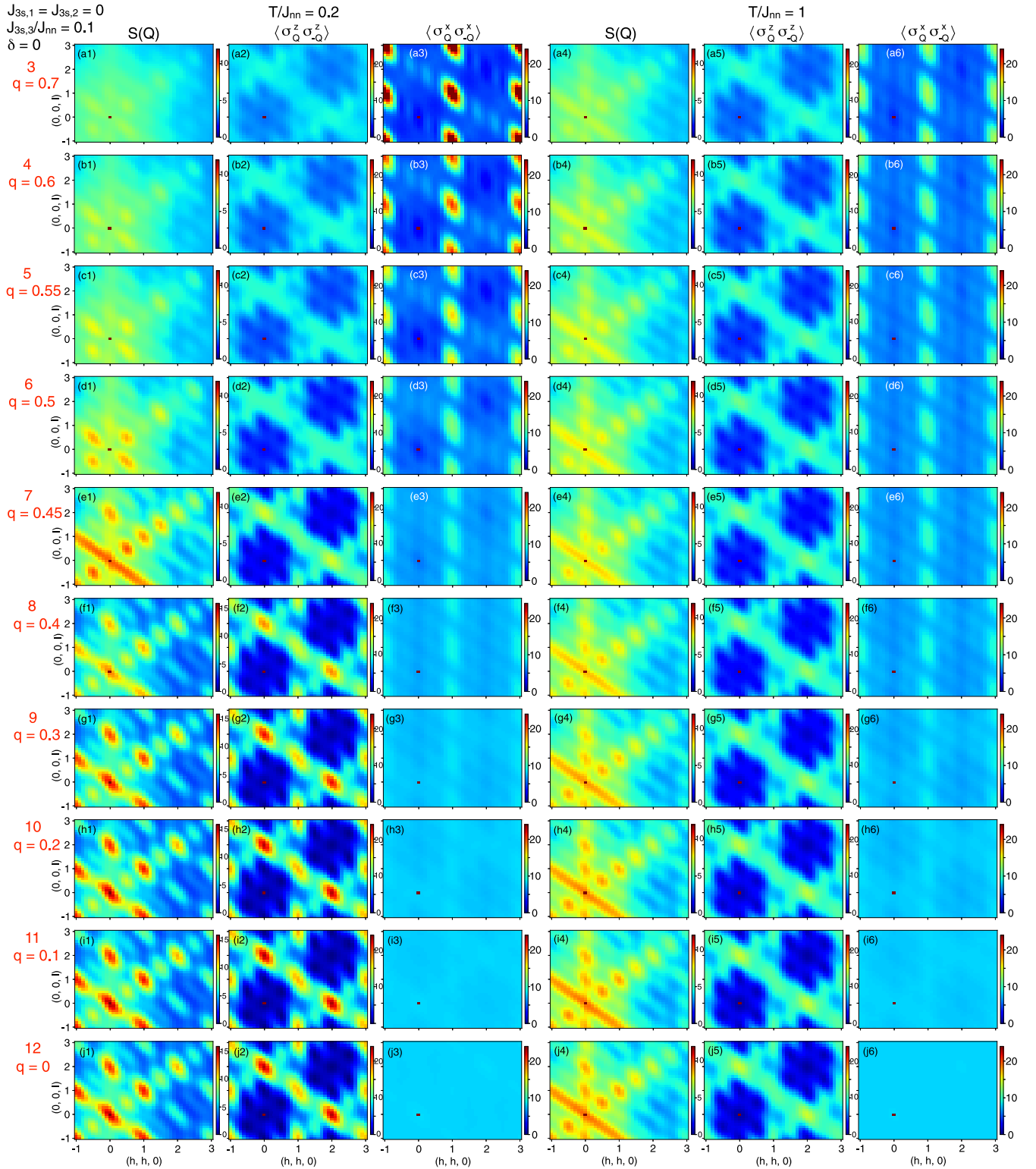


FIG. 13. Two-dimensional slices of (w1,w4) $S(\mathbf{Q})$, (w2,w5) $\langle \sigma_Q^z \sigma_{-Q}^z \rangle$, and (w3,w6) $\langle \sigma_Q^x \sigma_{-Q}^x \rangle$ [$w=a-j$] in the plane $\mathbf{Q} = (h, h, l)$ calculated by the 32-site simulations using the mTPQ state for $J_{3s,3}/J_{nn} = 0.1$ ($J_{3s,1} = J_{3s,2} = 0$) with parameters ($\delta = 0, q \geq 0$), the points 3–12 in Fig. 1. The 2D slice data at $T/J_{nn} = 0.2$ and 1 are shown in (w1)–(w3) and (w4)–(w6) [$w=a-j$], respectively.

sition at $T = 0$ in the thermodynamic limit $N \rightarrow \infty$ [31,32].

For $J_{3s,3}/J_{nn} = 0.1$ and ($\delta = 0, -0.7 < q < 0$), $S(\mathbf{Q})$ and $\langle \sigma_Q^\alpha \sigma_{-Q}^\alpha \rangle$ ($\alpha = z, x$) [Figs. 15(b–i)] continuously change in

the range $-0.7 < q < 0$. At $T/J_{nn} = 0.2$ and around $q = -0.5$ [Figs. 15(c1–e1,c2–e2,c3–e3)] they change very steeply as a function of q , which is consistent with the q dependence of $C(T)$ [Fig. 11(b)]. This steep change suggests a

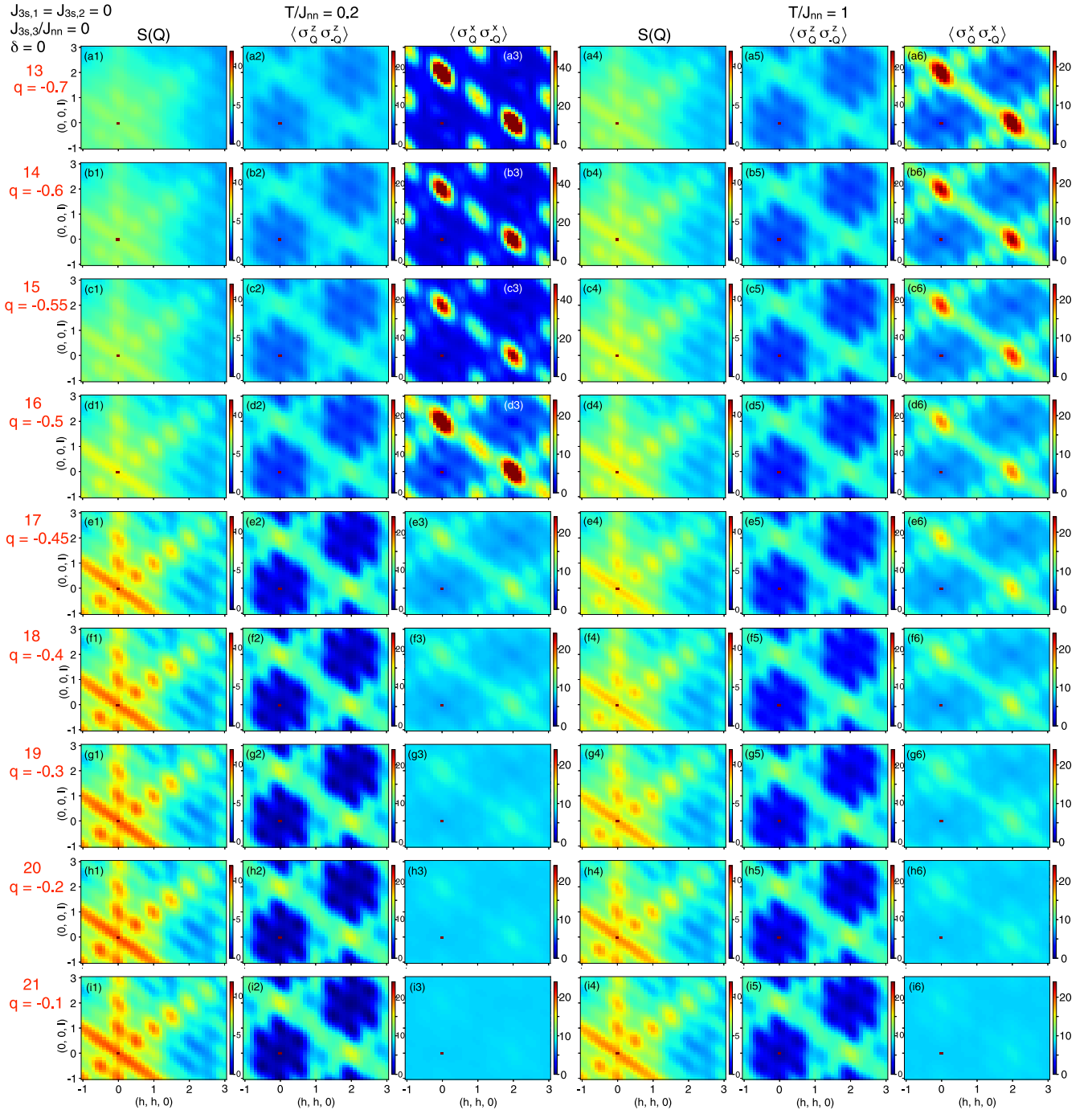


FIG. 14. Two-dimensional slices of (w1,w4) $S(\mathbf{Q})$, (w2,w5) $\langle \sigma_Q^z \sigma_{-Q}^z \rangle$, and (w3,w6) $\langle \sigma_Q^x \sigma_{-Q}^x \rangle$ [$w=a-i$] in the plane $\mathbf{Q} = (h, h, l)$ calculated by the 32-site simulations using the mTPQ state for $J_{3s,3}/J_{nn} = 0$ ($J_{3s,1} = J_{3s,2} = 0$) with parameters ($\delta = 0, q < 0$), the points 13–21 in Fig. 1. The 2D slice data at $T/J_{nn} = 0.2$ and 1 are shown in (w1)–(w3) and (w4)–(w6) [$w=a-i$], respectively.

first-order phase transition at $T = 0$ because the variation of $\langle \sigma_Q^x \sigma_{-Q}^x \rangle$ [Figs. 15(c3–e3)] is as steep as that for $J_{3s,3}/J_{nn} = 0$ [Figs. 14(c3–e3)]. In contrast, $S(\mathbf{Q})$ and $\langle \sigma_Q^\alpha \sigma_{-Q}^\alpha \rangle$ ($\alpha = z, x$) for $J_{3s,3}/J_{nn} = 0.1$ vary much more gradually around $q = 0.5$ at $T/J_{nn} = 0.2$ [Figs. 13(c1–e1, c2–e2, c3–e3)], which is consistent with the corresponding q dependence of $C(T)$ [Fig. 11(a)]. These suggest a possibility that at $T = 0$ there is another disordered ground state in the vicinity of $(\delta, q) = (0, 0.5)$, i.e., between the QSI and 3D-PAF ($q > 0$)

states, in the quantum phase diagram with $J_{3s,3}/J_{nn} = 0.1$ (Fig. 1).

4. Results of $C(T)$, $S(T)$, and $S(\mathbf{Q})$ for $\delta \neq 0$

To complement the simulation results on the q axis shown in Secs. IVC1–IVC3 a few 32-site simulations using the TPQ states with the eight sets of the parameters ($\delta = \pm 0.1, q$), the points 22–29 in Fig. 1, were carried out

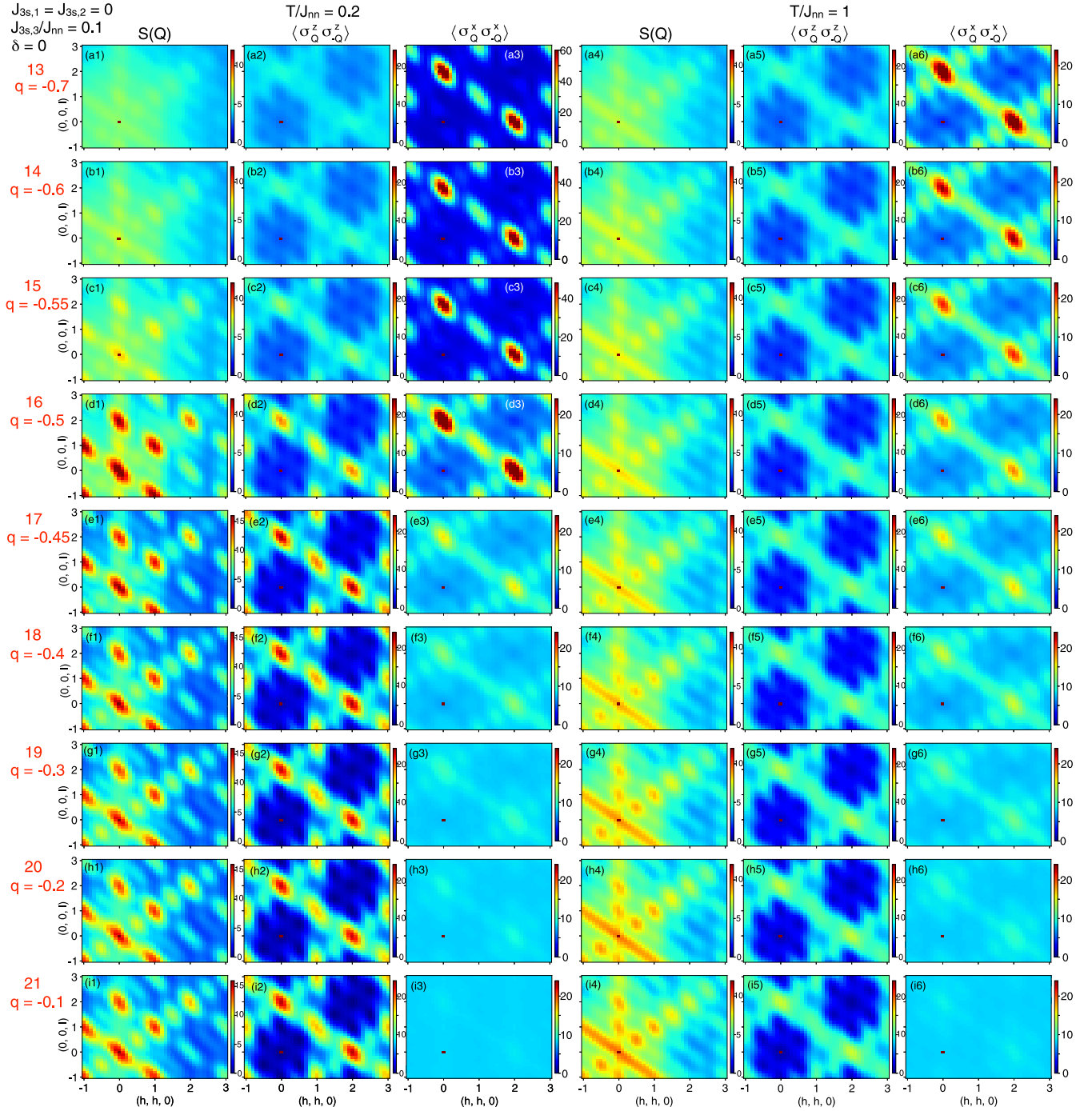


FIG. 15. Two-dimensional slices of (w1,w4) $S(\mathbf{Q})$, (w2,w5) $\langle \sigma_Q^z \sigma_{-Q}^z \rangle$, and (w3,w6) $\langle \sigma_Q^x \sigma_{-Q}^x \rangle$ [$w=a-i$] in the plane $\mathbf{Q} = (h, h, l)$ calculated by the 32-site simulations using the mTPQ state for $J_{3s,3}/J_{nn} = 0.1$ ($J_{3s,1} = J_{3s,2} = 0$) with parameters ($\delta = 0, q < 0$), the points 13–21 in Fig. 1. The 2D slice data at $T/J_{nn} = 0.2$ and 1 are shown in (w1)–(w3) and (w4)–(w6) [$w=a-i$], respectively.

for $J_{3s,3}/J_{nn} = 0$ and 0.1 ($J_{3s,1} = J_{3s,2} = 0$). These results are presented in Appendix E.

V. DISCUSSION

An answer to the initial question “why does $S(\mathbf{Q})$ of TTO show the spin correlations with $\mathbf{k} \sim (\frac{1}{2}, \frac{1}{2}, \frac{1}{2})$?” has been obtained by the results of the CMC simulations and the quantum simulations using the TPQ states to a certain extent. It

is an effect of one of the three-spin interactions, the $i = 3$ term of \mathcal{H}_{3s} [Eq. (3)]. This answer seems to provide basic understanding of TTO because of the following affirmative background reasoning or/and narratives. The three-spin interaction term is naturally expected from a perturbation expansion via virtual CF excitations [35,40]. The magnitude of $J_{3s,3}$ is consistent with this perturbation theory. Since the coupling constant $J_{3s,3}$ is an order smaller than J_{nn} , the three-spin interaction affects the spin correlations only at low temper-

atures and only if the system is located close to classical phase boundaries of the three states: the SI state, the 3D-PAF ($q > 0$) quadrupole-ordered state, and the state possessing both the quadrupole and magnetic orders. This proximity to the phase boundaries may have a profound theoretical meaning [43,57,70]. In the CMC simulation, where thermal fluctuations disappear at $T = 0$, the spin correlations with $\mathbf{k} \sim (\frac{1}{2}, \frac{1}{2}, \frac{1}{2})$ appear in the intermediate temperature ranges. In contrast, the quantum simulation suggests that the spin correlations exist down to $T = 0$ owing to quantum fluctuations.

However, there remain unresolved problems, mainly because the simulation methods are far from perfect. Although there are obviously the peaked structures with $\mathbf{k} \sim (\frac{1}{2}, \frac{1}{2}, \frac{1}{2})$ in the simulated $S(\mathbf{Q})$, these do not quantitatively reproduce the experimentally observed $S(\mathbf{Q})$. It is likely that the number of model parameters has to be increased for better fitting. The small size effect of the 32-site quantum simulation makes its results obscure and its interpretation difficult especially at low temperatures. As discussed in Ref. [35] the modeling of TTO is a nontrivial problem. In this work, we deal with the excited CF doublet state perturbatively, i.e., state vectors in the Hilbert space consisting of one doublet state per site. A larger Hilbert space, i.e., two doublet states per site may have to be taken into account [71]. Therefore, much work will have to be performed to solve the conundrum of TTO.

The electric quadrupole (multipole) operators represent the deformation of the f -electron charge density of Tb^{3+} , and inevitably couple to displacements of surrounding atoms [33,72–75]. An interesting point of the quantum simulation results is that the quadrupole correlations coexist with the spin correlations [Figs. 13(c1–c3,d1–d3)]. If this is really the case for QSL samples of TTO, it will be fascinating to observe these quadrupole correlations or/and correlated lattice deformations associated with them, which is a challenging experimental task.

Several neutron scattering experiments were performed on TTO samples, of which stoichiometries are mostly unknown. They showed that spin correlations are clearly seen in energy-resolution-limited (nominally and instrument-dependent) elastic scattering at low temperatures. Spin correlations were reported to show many features including the three main features: magnetic SRO with $\mathbf{k} \sim (\frac{1}{2}, \frac{1}{2}, \frac{1}{2})$ [76–79], pinch-point-like structures at $\mathbf{k} \sim \mathbf{0}$ [77,78], and tiny Bragg reflections at $\mathbf{k} = (\frac{1}{2}, \frac{1}{2}, \frac{1}{2})$ and $\mathbf{k} = \mathbf{0}$ [24,27]. These may have to be revisited using well-controlled TTO samples and under well-tuned instrumental conditions.

It should be noted that the spin correlations, i.e., neutron scattering intensity patterns, reported in Refs. [77,78] are significantly different from those shown in Fig. 5, which has been puzzling for many years. On the other hand, the intensity patterns [77,78] show a similarity to those of the related pyrochlore magnet $\text{Tb}_2\text{Hf}_2\text{O}_7$, which has a strongly disordered structure [21]. These experimental facts possibly suggest that there is another QSL state in TTO which is changed by a structural disorder for a stoichiometry range $x > 0.04$, where QO is suppressed and the system remains paramagnetic down to the lowest temperatures [Fig. 4(b) in [25]]. If one assumes that there are site-random quadrupole moments $\langle \sigma_r^+ \rangle$ fixed by defects, QO can be suppressed by a random-field mechanism [80,81]. The site random $\langle \sigma_r^+ \rangle$

may give rise to magnetic bond-random interactions due to the three-spin interaction [Eq. (14)] and significantly modify spin correlations. At present, disorder effects in pyrochlore magnets are little understood.

VI. CONCLUSIONS

We have studied spin correlations characterized by the modulation wave vector $\mathbf{k} \sim (\frac{1}{2}, \frac{1}{2}, \frac{1}{2})$ observed in the putative QSL pyrochlore magnet $\text{Tb}_{2+x}\text{Ti}_{2-x}\text{O}_{7+y}$ [26,34]. Since they could not be accounted for by adding further-neighbor magnetic interactions to the NN pseudospin- $\frac{1}{2}$ Hamiltonian proposed in Ref. [27], in this work we have explored another possibility of adding a three-spin interaction term of a form $\sigma_r^\pm \sigma_r^z \sigma_{r'}^z$, which is a correction to the Hamiltonian due to the low crystal-field excitation.

Classical MC simulation and quantum simulation using the TPQ states are applied to analyze experimentally observed structure factor $S(\mathbf{Q})$. The simulation results show that spin correlations with $\mathbf{k} \sim (\frac{1}{2}, \frac{1}{2}, \frac{1}{2})$, coexisting with electric quadrupole correlations with $\mathbf{k} \sim \mathbf{0}$, are induced at low temperatures by the three-spin interaction. The results suggest that the QSL state of $\text{Tb}_{2+x}\text{Ti}_{2-x}\text{O}_{7+y}$ is located close to phase boundaries of the spin-ice, quadrupole-ordered, and both quadrupole- and magnetic-ordered states in the classical approximation, and that the three-spin interaction brings about a quantum disordered ground state with both spin and quadrupole correlations.

As a by-product, the quantum simulation roughly reproduces the puzzling behavior of specific heat $C(T) \sim \text{const}$, which was experimentally observed at low temperatures. Therefore, we conclude that the classical and quantum simulation results suggest that the effective Hamiltonian minimally describing $\text{Tb}_{2+x}\text{Ti}_{2-x}\text{O}_{7+y}$ is $\mathcal{H}_0 + \mathcal{H}_{3s}$ [Eqs. (1) and (3)] with $J_{3s,1} = J_{3s,2} = 0$, $J_{3s,3}/J_{\text{nn}} \sim 0.1$ (or -0.1) and the parameters (δ, q) in the region which is enclosed by the red dashed line in Fig. 1. A novel viewpoint of the QSL state of $\text{Tb}_{2+x}\text{Ti}_{2-x}\text{O}_{7+y}$ and/or elaborate theories which quantitatively reproduce the spin correlations will be hopefully constructed based on this work.

ACKNOWLEDGMENTS

This work was supported by JSPS KAKENHI Grant No. 25400345. The neutron scattering performed using ILL IN5 (France) was transferred from JRR-3M HER (proposal 11567, 15545) with the approval of ISSP, University of Tokyo, and JAEA, Tokai, Japan. The neutron scattering experiments at J-PARC AMATERAS were carried out under a research Project No. 2016A0327. The computation was performed on supercomputers at ISSP University of Tokyo, ITC Nagoya University, and Hokkaido University.

APPENDIX A: CF GROUND-STATE DOUBLET, LATTICE SITES, ETC.

The CF ground-state doublet of TTO at each site is written by

$$|\pm 1\rangle_{\text{D}} = |A\rangle \mp |4\rangle \pm |B\rangle \mp |1\rangle + |C\rangle \pm |2\rangle \mp |D\rangle \pm |5\rangle, \quad (\text{A1})$$

TABLE I. Four crystallographic sites \mathbf{d}_ν and their local symmetry axes \mathbf{x}_ν , \mathbf{y}_ν , and \mathbf{z}_ν . These coordinates are defined using (global) cubic XYZ axes shown in Fig. 1(a). The four sites \mathbf{d}_ν are illustrated by vertices with light blue numbers ($\nu = 1-4$) of a tetrahedron in Fig. 1(a).

ν	\mathbf{d}_ν	\mathbf{x}_ν	\mathbf{y}_ν	\mathbf{z}_ν
1	$\frac{1}{4}(0, 0, 0)$	$\frac{1}{\sqrt{6}}(1, 1, -2)$	$\frac{1}{\sqrt{2}}(-1, 1, 0)$	$\frac{1}{\sqrt{3}}(1, 1, 1)$
2	$\frac{1}{4}(0, 1, 1)$	$\frac{1}{\sqrt{6}}(1, -1, 2)$	$\frac{1}{\sqrt{2}}(-1, -1, 0)$	$\frac{1}{\sqrt{3}}(1, -1, -1)$
3	$\frac{1}{4}(1, 0, 1)$	$\frac{1}{\sqrt{6}}(-1, 1, 2)$	$\frac{1}{\sqrt{2}}(1, 1, 0)$	$\frac{1}{\sqrt{3}}(-1, 1, -1)$
4	$\frac{1}{4}(1, 1, 0)$	$\frac{1}{\sqrt{6}}(-1, -1, -2)$	$\frac{1}{\sqrt{2}}(1, -1, 0)$	$\frac{1}{\sqrt{3}}(-1, -1, 1)$

where $|m\rangle$ stands for the $|J = 6, m\rangle$ state within a *JLS* multiplet [82]. The coefficients of Eq. (A1) are $A = 0.9581$, $B = 0.1284$, $C = 0.1210$, and $D = 0.2256$ using the CF parameters of Ref. [83]. Magnetic-dipole and electric-quadrupole moment operators [84] within $|\pm 1\rangle_D$ are proportional to the Pauli matrices σ^α ($\alpha = x, y, z$) and the unit matrix [28,85]. The magnetic dipole moment operators are given by

$$J_x = J_y = 0, \\ J_z = -(4A^2 + B^2 - 2C^2 - 5D^2)\sigma^z. \quad (\text{A2})$$

The electric quadrupole moment operators are expressed as

$$\frac{1}{2}[3J_z^2 - J(J+1)] = 3A^2 - \frac{39}{2}B^2 - 15C^2 + \frac{33}{2}D^2, \\ \frac{\sqrt{3}}{2}[J_x^2 - J_y^2] = \left(-\frac{21\sqrt{3}}{2}B^2 + 9\sqrt{10}AC\right)\sigma^x, \\ \frac{\sqrt{3}}{2}[J_x J_y + J_y J_x] = -\left(-\frac{21\sqrt{3}}{2}B^2 + 9\sqrt{10}AC\right)\sigma^y, \\ \frac{\sqrt{3}}{2}[J_z J_x + J_x J_z] = -\left(3\sqrt{30}BC + 9\sqrt{\frac{33}{2}}AD\right)\sigma^x, \\ \frac{\sqrt{3}}{2}[J_y J_z + J_z J_y] = -\left(3\sqrt{30}BC + 9\sqrt{\frac{33}{2}}AD\right)\sigma^y. \quad (\text{A3})$$

The operators σ_r^α of Eq. (1) act on $|\pm 1\rangle_D$ at each pyrochlore lattice site $\mathbf{r} = \mathbf{t}_n + \mathbf{d}_\nu$, where \mathbf{t}_n is an fcc translation vector and \mathbf{d}_ν ($\nu = 1, 2, 3$, and 4) are four crystallographic sites in the unit cell. Coordinates of the sites \mathbf{d}_ν and their local axes \mathbf{x}_ν , \mathbf{y}_ν , and \mathbf{z}_ν are listed in Table I. Under these definitions the effective Hamiltonian is described by Eq. (1) with the phases $\phi_{r,r'}$ listed in Table II [31].

TABLE II. Phases $\phi_{r,r'}$ of the quadrupole interactions $J_{mn}2q \exp[i2\phi_{r,r'}]\sigma_r^+ \sigma_{r'}^+ + \text{H.c.}$ [Eq. (1)], where $\mathbf{r} = \mathbf{t}_n + \mathbf{d}_\nu$ and $\mathbf{r}' = \mathbf{t}_{n'} + \mathbf{d}_{\nu'}$.

ν	ν'	$\mathbf{r}' - \mathbf{r}$	$\phi_{r,r'}/(\frac{2\pi}{3})$
1	2	$\frac{1}{4}(0, 1, 1)$	-1
1	3	$\frac{1}{4}(1, 0, 1)$	1
1	4	$\frac{1}{4}(1, 1, 0)$	0
2	3	$\frac{1}{4}(1, -1, 0)$	0
2	4	$\frac{1}{4}(1, 0, -1)$	1
3	4	$\frac{1}{4}(0, 1, -1)$	-1

TABLE III. Phases $\phi_{r,r',r''}^{(1)}$ of the type $i = 1$ three-spin interaction $J_{3s,1} \exp[i\phi_{r,r',r''}^{(1)}]\sigma_r^+ \sigma_{r'}^z \sigma_{r''}^z + \text{H.c.}$ [Eq. (3)], where $\mathbf{r} = \mathbf{t}_n + \mathbf{d}_\nu$, $\mathbf{r}' = \mathbf{t}_{n'} + \mathbf{d}_{\nu'}$, and $\mathbf{r}'' = \mathbf{t}_{n''} + \mathbf{d}_{\nu''}$. The site triplet $\langle \mathbf{r}, \mathbf{r}', \mathbf{r}'' \rangle$ of the first line is illustrated in Fig. 2(a).

ν	ν'	ν''	$\mathbf{r}' - \mathbf{r}$	$\mathbf{r}'' - \mathbf{r}$	$\phi_{r,r',r''}^{(1)}/(\frac{2\pi}{3})$
1	2	2	$\frac{1}{4}(0, 1, 1)$	$\frac{1}{4}(0, -1, -1)$	-1
1	3	3	$\frac{1}{4}(1, 0, 1)$	$\frac{1}{4}(-1, 0, -1)$	1
1	4	4	$\frac{1}{4}(1, 1, 0)$	$\frac{1}{4}(-1, -1, 0)$	0
2	1	1	$\frac{1}{4}(0, 1, 1)$	$\frac{1}{4}(0, -1, -1)$	-1
2	3	3	$\frac{1}{4}(1, -1, 0)$	$\frac{1}{4}(-1, 1, 0)$	0
2	4	4	$\frac{1}{4}(1, 0, -1)$	$\frac{1}{4}(-1, 0, 1)$	1
3	1	1	$\frac{1}{4}(1, 0, 1)$	$\frac{1}{4}(-1, 0, -1)$	1
3	2	2	$\frac{1}{4}(1, -1, 0)$	$\frac{1}{4}(-1, 1, 0)$	0
3	4	4	$\frac{1}{4}(0, 1, -1)$	$\frac{1}{4}(0, -1, 1)$	-1
4	1	1	$\frac{1}{4}(1, 1, 0)$	$\frac{1}{4}(-1, -1, 0)$	0
4	2	2	$\frac{1}{4}(1, 0, -1)$	$\frac{1}{4}(-1, 0, 1)$	1
4	3	3	$\frac{1}{4}(0, 1, -1)$	$\frac{1}{4}(0, -1, 1)$	-1

TABLE IV. Phases $\phi_{r,r',r''}^{(2)}$ of the type $i = 2$ three-spin interaction $J_{3s,2} \exp[i\phi_{r,r',r''}^{(2)}]\sigma_r^+ \sigma_{r'}^z \sigma_{r''}^z + \text{H.c.}$ [Eq. (3)], where $\mathbf{r} = \mathbf{t}_n + \mathbf{d}_\nu$, $\mathbf{r}' = \mathbf{t}_{n'} + \mathbf{d}_{\nu'}$, and $\mathbf{r}'' = \mathbf{t}_{n''} + \mathbf{d}_{\nu''}$. The site triplet $\langle \mathbf{r}, \mathbf{r}', \mathbf{r}'' \rangle$ of the first line is illustrated in Fig. 2(b).

ν	ν'	ν''	$\mathbf{r}' - \mathbf{r}$	$\mathbf{r}'' - \mathbf{r}$	$\phi_{r,r',r''}^{(2)}/(\frac{2\pi}{3})$
1	2	3	$\frac{1}{4}(0, 1, 1)$	$\frac{1}{4}(1, 0, 1)$	0
1	2	3	$\frac{1}{4}(0, -1, -1)$	$\frac{1}{4}(-1, 0, -1)$	0
1	2	4	$\frac{1}{4}(0, -1, -1)$	$\frac{1}{4}(-1, -1, 0)$	1
1	2	4	$\frac{1}{4}(0, 1, 1)$	$\frac{1}{4}(1, 1, 0)$	1
1	3	4	$\frac{1}{4}(-1, 0, -1)$	$\frac{1}{4}(-1, -1, 0)$	-1
1	3	4	$\frac{1}{4}(1, 0, 1)$	$\frac{1}{4}(1, 1, 0)$	-1
2	1	3	$\frac{1}{4}(0, -1, -1)$	$\frac{1}{4}(1, -1, 0)$	1
2	1	3	$\frac{1}{4}(0, 1, 1)$	$\frac{1}{4}(-1, 1, 0)$	1
2	1	4	$\frac{1}{4}(0, -1, -1)$	$\frac{1}{4}(1, 0, -1)$	0
2	1	4	$\frac{1}{4}(0, 1, 1)$	$\frac{1}{4}(-1, 0, 1)$	0
2	3	4	$\frac{1}{4}(-1, 1, 0)$	$\frac{1}{4}(-1, 0, 1)$	-1
2	3	4	$\frac{1}{4}(1, -1, 0)$	$\frac{1}{4}(1, 0, -1)$	-1
3	1	2	$\frac{1}{4}(-1, 0, -1)$	$\frac{1}{4}(-1, 1, 0)$	-1
3	1	2	$\frac{1}{4}(1, 0, 1)$	$\frac{1}{4}(1, -1, 0)$	-1
3	1	4	$\frac{1}{4}(-1, 0, -1)$	$\frac{1}{4}(0, 1, -1)$	0
3	1	4	$\frac{1}{4}(1, 0, 1)$	$\frac{1}{4}(0, -1, 1)$	0
3	2	4	$\frac{1}{4}(-1, 1, 0)$	$\frac{1}{4}(0, 1, -1)$	1
3	2	4	$\frac{1}{4}(1, -1, 0)$	$\frac{1}{4}(0, -1, 1)$	1
4	1	2	$\frac{1}{4}(-1, -1, 0)$	$\frac{1}{4}(-1, 0, 1)$	-1
4	1	2	$\frac{1}{4}(1, 1, 0)$	$\frac{1}{4}(1, 0, -1)$	-1
4	1	3	$\frac{1}{4}(-1, -1, 0)$	$\frac{1}{4}(0, -1, 1)$	1
4	1	3	$\frac{1}{4}(1, 1, 0)$	$\frac{1}{4}(0, 1, -1)$	1
4	2	3	$\frac{1}{4}(-1, 0, 1)$	$\frac{1}{4}(0, -1, 1)$	0
4	2	3	$\frac{1}{4}(1, 0, -1)$	$\frac{1}{4}(0, 1, -1)$	0

TABLE V. Phases $\phi_{\mathbf{r},\mathbf{r}',\mathbf{r}''}^{(3)}$ of the type $i = 3$ three-spin interaction $J_{3s,3} \exp[i\phi_{\mathbf{r},\mathbf{r}',\mathbf{r}''}^{(3)}] \sigma_{\mathbf{r}}^+ \sigma_{\mathbf{r}'}^z \sigma_{\mathbf{r}''}^z + \text{H.c.}$ [Eq. (3)], where $\mathbf{r} = \mathbf{t}_n + \mathbf{d}_v$, $\mathbf{r}' = \mathbf{t}_{n'} + \mathbf{d}_{v'}$, and $\mathbf{r}'' = \mathbf{t}_{n''} + \mathbf{d}_{v''}$. The site triplet $(\mathbf{r}, \mathbf{r}', \mathbf{r}'')$ of the first line is illustrated in Fig. 2(c).

v	v'	v''	$\mathbf{r}' - \mathbf{r}$	$\mathbf{r}'' - \mathbf{r}$	$\phi_{\mathbf{r},\mathbf{r}',\mathbf{r}''}^{(3)} / (\frac{2\pi}{3})$
1	2	3	$\frac{1}{4}(0, -1, -1)$	$\frac{1}{4}(1, 0, 1)$	0
1	2	3	$\frac{1}{4}(0, 1, 1)$	$\frac{1}{4}(-1, 0, -1)$	0
1	2	4	$\frac{1}{4}(0, -1, -1)$	$\frac{1}{4}(1, 1, 0)$	1
1	2	4	$\frac{1}{4}(0, 1, 1)$	$\frac{1}{4}(-1, -1, 0)$	1
1	3	4	$\frac{1}{4}(-1, 0, -1)$	$\frac{1}{4}(1, 1, 0)$	-1
1	3	4	$\frac{1}{4}(1, 0, 1)$	$\frac{1}{4}(-1, -1, 0)$	-1
2	1	3	$\frac{1}{4}(0, -1, -1)$	$\frac{1}{4}(-1, 1, 0)$	1
2	1	3	$\frac{1}{4}(0, 1, 1)$	$\frac{1}{4}(1, -1, 0)$	1
2	1	4	$\frac{1}{4}(0, -1, -1)$	$\frac{1}{4}(-1, 0, 1)$	0
2	1	4	$\frac{1}{4}(0, 1, 1)$	$\frac{1}{4}(1, 0, -1)$	0
2	3	4	$\frac{1}{4}(-1, 1, 0)$	$\frac{1}{4}(1, 0, -1)$	-1
2	3	4	$\frac{1}{4}(1, -1, 0)$	$\frac{1}{4}(-1, 0, 1)$	-1
3	1	2	$\frac{1}{4}(-1, 0, -1)$	$\frac{1}{4}(1, -1, 0)$	-1
3	1	2	$\frac{1}{4}(1, 0, 1)$	$\frac{1}{4}(-1, 1, 0)$	-1
3	1	4	$\frac{1}{4}(-1, 0, -1)$	$\frac{1}{4}(0, -1, 1)$	0
3	1	4	$\frac{1}{4}(1, 0, 1)$	$\frac{1}{4}(0, 1, -1)$	0
3	2	4	$\frac{1}{4}(-1, 1, 0)$	$\frac{1}{4}(0, -1, 1)$	1
3	2	4	$\frac{1}{4}(1, -1, 0)$	$\frac{1}{4}(0, 1, -1)$	1
4	1	2	$\frac{1}{4}(-1, -1, 0)$	$\frac{1}{4}(1, 0, -1)$	-1
4	1	2	$\frac{1}{4}(1, 1, 0)$	$\frac{1}{4}(-1, 0, 1)$	-1
4	1	3	$\frac{1}{4}(-1, -1, 0)$	$\frac{1}{4}(0, 1, -1)$	1
4	1	3	$\frac{1}{4}(1, 1, 0)$	$\frac{1}{4}(0, -1, 1)$	1
4	2	3	$\frac{1}{4}(-1, 0, 1)$	$\frac{1}{4}(0, 1, -1)$	0
4	2	3	$\frac{1}{4}(1, 0, -1)$	$\frac{1}{4}(0, -1, 1)$	0

APPENDIX B: THREE-SPIN INTERACTION

Following Refs. [35,40], the three-spin interactions consist of terms with a form $(c\sigma_{\mathbf{r}}^+ + c^*\sigma_{\mathbf{r}}^-)\sigma_{\mathbf{r}'}^z\sigma_{\mathbf{r}''}^z$, where the site triplet $(\mathbf{r}, \mathbf{r}', \mathbf{r}'')$ satisfies geometrical conditions: $(\mathbf{r}, \mathbf{r}')$ and $(\mathbf{r}, \mathbf{r}'')$ are NN site pairs, the site \mathbf{r}' is different from \mathbf{r}'' . Under these conditions the three-spin interaction term can be expressed by Eq. (3) with unknown phases $\phi_{\mathbf{r},\mathbf{r}',\mathbf{r}''}^{(i)}$. By imposing the condition that the three-spin interaction term is invariant under the space-group symmetry ($Fd\bar{3}m$, No. 227), it is not difficult to determine the phases using the symmetry method employed for the two-spin interaction term of pyrochlore magnets [31,86,87]. The phases $\phi_{\mathbf{r},\mathbf{r}',\mathbf{r}''}^{(i)}$ with $i = 1, 2$, and 3 are listed in Tables III–V, respectively.

APPENDIX C: CMC SIMULATION RESULTS: $S(\mathbf{Q})$ IN 3D-PAF ($q > 0$) PHASE $\delta \neq 0$

To complement the simulation results of $S(\mathbf{Q})$ shown in Figs. 8(i–n), we performed a few 16000-site CMC simulations with slightly different parameters: $\frac{J_{\text{nn}}}{J_{\text{nn}}+D_{\text{nn}}}(\delta, q) = (-0.1, 0.6)$ and $(0.1, 0.5)$, corresponding to the points 31 and 33 in Fig. 3, respectively. The three-spin interaction constants were fixed to $J_{3s,1} = J_{3s,2} = 0$ and $J_{3s,3} = 0, 0.1, 0.15$ K. Fig-

ures 16 and 17 show the resulting intensity maps of $S(\mathbf{Q})$ which were calculated with the parameters corresponding to the red circles in Figs. 6(a3) and 6(c3), respectively, and at two temperatures 0.2 and 0.35 K, below and above the phase transition temperature of the 3D-PAF ($q > 0$) LRO.

The calculated $S(\mathbf{Q})$ of Figs. 16(a–f) and 17(a–f) bear close resemblances to $S(\mathbf{Q})$ of Figs. 8(i–n). This is in parallel with the analyses of Ref. [27], in which the acceptable parameter range we proposed has the elongated shape (Fig. 3). Thus, we can conclude that the parameter sets used for Figs. 16(c,d) and 17(c,d) are also candidates for the further investigation. We note that $S(\mathbf{Q})$ maps of Figs. 16(a,c) and 17(a,c), which are obtained from simulations at 0.2 K with $J_{3s,3} = 0.15$ and 0.1, show certain difference from those of Figs. 8(i,k). This may be caused by high degeneracy due to proximity to the SI phase boundary, where the $S(\mathbf{Q})$ map is easily changed by small perturbations. To obtain better fit of the calculated $S(\mathbf{Q})$ to the observed $S(\mathbf{Q})$ of TTO, we have tried several parameter adjustments by adding small parameters: $J_{3s,1}$, $J_{3s,2}$, second- and third-neighbor magnetic exchange couplings (J_2 , J_3 , J_4 [34]). The fit, however, could not be improved.

APPENDIX D: CMC SIMULATION RESULTS: $S(\mathbf{Q})$ IN SI PHASE

Several 16000-site CMC simulations were performed to study effects of each three-spin interaction on $S(\mathbf{Q})$ on the SI phase sides of neighborhoods of the SI and 3D-PAF phase boundaries. Considering the results of Sec. IV B 2, the parameters (δ, q) were fixed to the two sets: $\frac{J_{\text{nn}}}{J_{\text{nn}}+D_{\text{nn}}}(\delta, q) = (0.0, 0.45)$ and $(0.0, -0.45)$, the points 38 and 41 in Fig. 3. The three-spin interaction constant was fixed to two typical values: $J_{3s,i} = 0.1$ and 0.15 K ($J_{3s,j \neq i} = 0$). Figure 18 shows the resulting intensity maps of $S(\mathbf{Q})$ which are calculated with the parameters corresponding to the red circles in Figs. 7(b1–b3), and at 0.2 and 0.35 K, below and above the specific heat peak. Figure 19 shows the resulting intensity maps of $S(\mathbf{Q})$ which are calculated with the parameters corresponding to the red circles in Figs. 7(e1–e3), and at 0.2 and 0.35 K, below and above the specific-heat peak. One can notice that statistical errors of $S(\mathbf{Q})$ at 0.2 K shown in Figs. 18 and 19 are much larger than those in Figs. 8 and 9. This indicates that pseudospin fluctuations are considerably slowed down in the SI phase within the CMC simulation.

When the three-spin interactions are set to zero, the calculated intensity maps with $\frac{J_{\text{nn}}}{J_{\text{nn}}+D_{\text{nn}}}q = 0.45$ and -0.45 , which are Figs. 18(m,n) and 19(m,n), respectively, show almost the same characteristics: the pinch-point structure of SI is seen around the Γ points (0,0,2) and (1,1,1), the intensity pattern becomes strengthened as temperature is lowered below the specific-heat peak. The intensity pattern is scarcely affected by the sign of the parameter q .

When the three-spin interactions are switched on, $S(\mathbf{Q})$ at 0.35 K [Figs. 18(b,d,f,h,j,l) and 19(b,d,f,h,j,l)] depend little on $J_{3s,i}$. On the other hand, $S(\mathbf{Q})$ at 0.2 K [Figs. 18(a,c,e,g,i,k) and 19(a,c,e,g,i,k)] show various intensity patterns depending on $J_{3s,i}$, which are attributable to the lifting of the degeneracy of the SI manifold. In relation to the analysis of TTO, there is only one somewhat interesting $S(\mathbf{Q})$ shown in Fig. 18(i), of which the parameters are $J_{3s,3} = 0.15$ K and $q > 0$. These

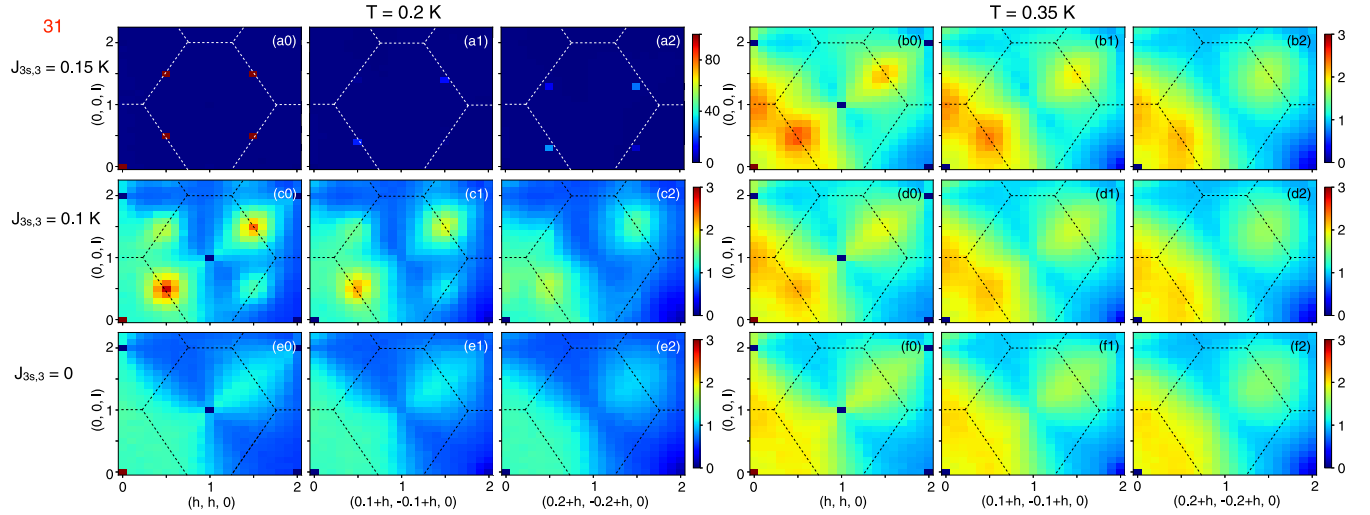


FIG. 16. Intensity maps of $S(\mathbf{Q})$ calculated by the 16000-site CMC simulations using parameters indicated by red circles shown in Fig. 6(a3) ($J_{3s,3}; J_{3s,1} = J_{3s,2} = 0$) and by the point 31 in Fig. 3 [$\frac{J_{nn}}{J_{nn}+D_{nn}}(\delta, q) = (-0.1, 0.6)$]. They are viewed by 2D slices of $\mathbf{Q} = (k+h, -k+h, l)$ with fixed $k = 0, 0.1, \text{ and } 0.2$, which are shown in (w0), (w1), and (w2) [$w=a-f$], respectively. They are calculated at two temperatures 0.2 K [(a), (c), (e)] and 0.35 K [(b), (d), (f)] below and above the phase transition temperature of the 3D-PAF ($q > 0$) LRO. Intensity maps for $J_{3s,3} = 0.15, 0.1, \text{ and } 0$ K [Fig. 6(a3)] are shown in (a,b), (c,d), and (e,f), respectively.

parameters are very close to the suggested range for the further investigation discussed in Sec. IV B 3.

APPENDIX E: OTHER RESULTS OF QUANTUM SIMULATION USING TPQ STATES: SPECIFIC HEAT, ENTROPY, AND $S(\mathbf{Q})$ FOR $\delta \neq 0$

To complement the simulation results on the q axis, a few 32-site simulations using the TPQ states with the eight sets of the parameters ($\delta = \pm 0.1, q$), the points 22–29 in Fig. 1, were carried out for $J_{3s,3}/J_{nn} = 0$ and 0.1 ($J_{3s,1} = J_{3s,2} = 0$). Temperature dependencies of specific heat $C(T)$ and entropy

$S(T)$ are plotted in Figs. 20 and 21. Two-dimensional slices of $S(\mathbf{Q})$ and $\langle \sigma_Q^\alpha \sigma_{-Q}^\alpha \rangle$ ($\alpha = z, x$) calculated with $q > 0$, the points 22–25 in Fig. 1, for $J_{3s,3}/J_{nn} = 0$ and 0.1 are shown in Figs. 22 and 23, respectively. Two-dimensional slices of $S(\mathbf{Q})$ and $\langle \sigma_Q^\alpha \sigma_{-Q}^\alpha \rangle$ ($\alpha = z, x$) calculated with $q < 0$, the points 26–29 in Fig. 1, for $J_{3s,3}/J_{nn} = 0$ and 0.1 are shown in Figs. 24 and 25, respectively.

For $J_{3s,3}/J_{nn} = 0$, since \mathcal{H}_0 is invariant under the transformation of rotating σ_r about the local z_r axis by $\pi/2$ and $q \rightarrow -q$, $C(T)$ and $S(T)$ curves with $q > 0$ [Figs. 20(a,c)] are almost the same as corresponding curves with $q < 0$ [Figs. 20(b,d)]. For $J_{3s,3} \neq 0$ the invariance does not

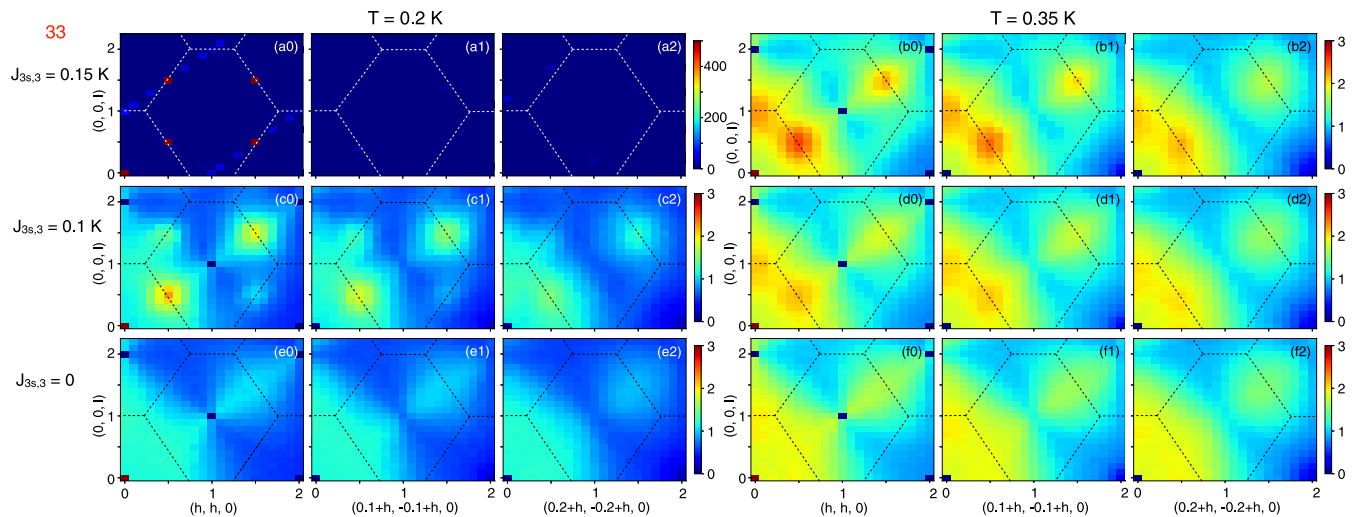


FIG. 17. Intensity maps of $S(\mathbf{Q})$ calculated by the 16000-site CMC simulations using parameters indicated by red circles shown in Fig. 6(c3) ($J_{3s,3}; J_{3s,1} = J_{3s,2} = 0$) and by the point 33 in Fig. 3 [$\frac{J_{nn}}{J_{nn}+D_{nn}}(\delta, q) = (0.1, 0.5)$]. They are viewed by 2D slices of $\mathbf{Q} = (k+h, -k+h, l)$ with fixed $k = 0, 0.1, \text{ and } 0.2$, which are shown in (w0), (w1), and (w2) [$w=a-f$], respectively. They are calculated at two temperatures 0.2 K [(a), (c), (e)] and 0.35 K [(b), (d), (f)] below and above the phase transition temperature of the 3D-PAF ($q > 0$) LRO. Intensity maps for $J_{3s,3} = 0.15, 0.1, \text{ and } 0$ K [Fig. 6(c3)] are shown in (a,b), (c,d), and (e,f), respectively.

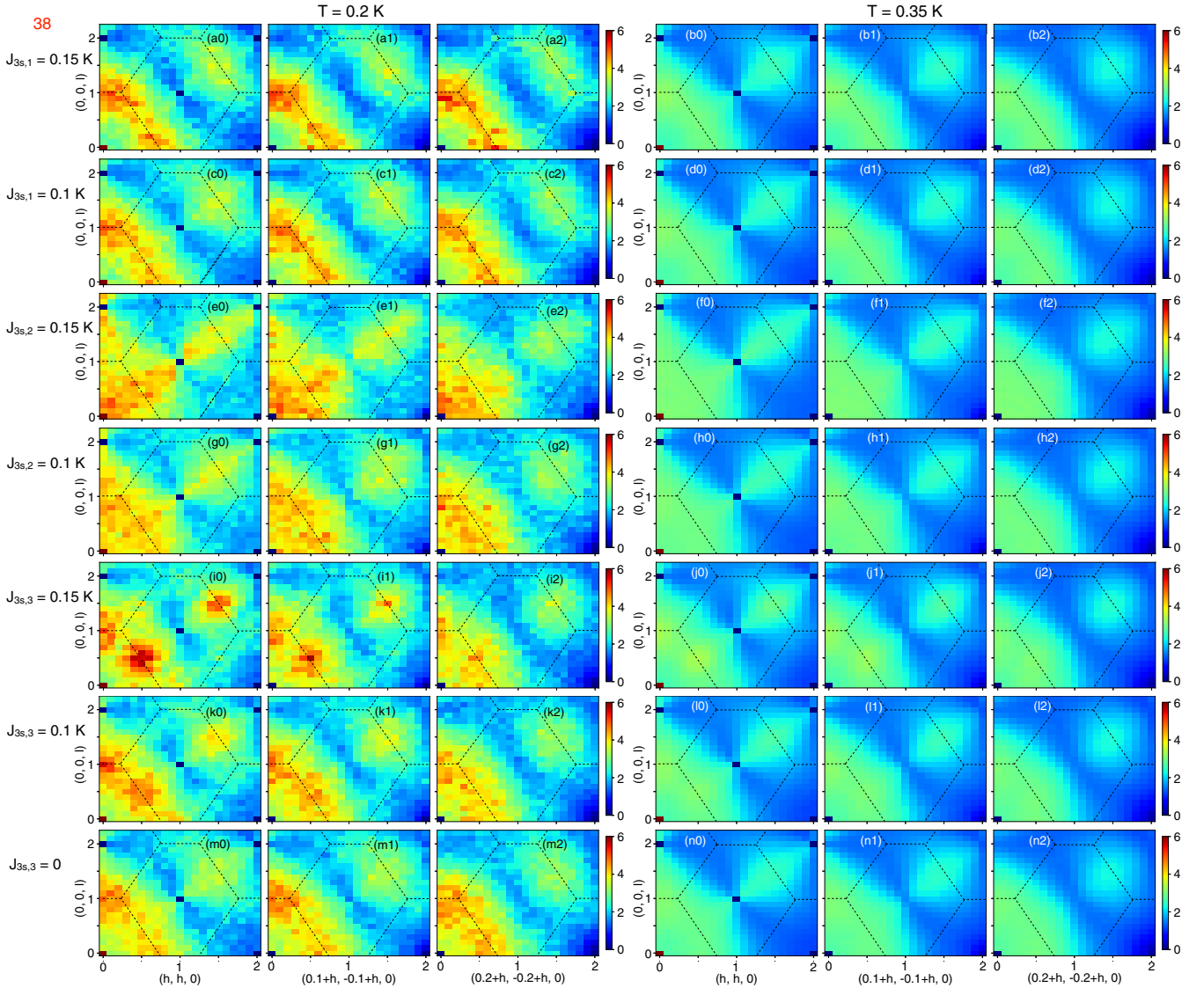


FIG. 18. Intensity maps of $S(\mathbf{Q})$ calculated by the 16000-site CMC simulations using parameters indicated by red circles shown in Figs. 7(b1–b3) ($J_{3s,i}$; $i = 1, 2, 3$; $J_{3s,j \neq i} = 0$) and by the point 38 in Fig. 3 [$\frac{J_{nn}}{J_{nn}+D_{nn}}(\delta, q) = (0.0, 0.45)$]. They are viewed by 2D slices of $\mathbf{Q} = (k+h, -k+h, l)$ with fixed $k = 0, 0.1$, and 0.2 , which are shown in (w0), (w1), and (w2) [$w=a-n$], respectively. They are calculated at two temperatures 0.2 K (a,c,e,g,i,k,m) and 0.35 K (b,d,f,h,j,l,n), below and above the specific-heat peak. Intensity maps for $J_{3s,1} = 0.15$ and 0.1 K [Fig. 7(b1)] are shown in (a,b) and (c,d), respectively. Intensity maps for $J_{3s,2} = 0.15$ and 0.1 K [Fig. 7(b2)] are shown in (e,f) and (g,h), respectively. Intensity maps for $J_{3s,3} = 0.15, 0.1$, and 0 K [Fig. 7(b3)] are shown in (i,j), (k,l), and (m,n), respectively.

hold, resulting in $C(T, \delta, q) \neq C(T, \delta, -q)$ [Figs. 21(a,b)] and $S(T, \delta, q) \neq S(T, \delta, -q)$ [Figs. 21(c,d)].

For $J_{3s,3}/J_{nn} = 0$, $S(\mathbf{Q})$ and $\langle \sigma_Q^z \sigma_{-Q}^z \rangle$ with $q > 0$ [Figs. 22(a1–d1,a4–d4) and 22(a2–d2,a5–d5)] are the same as those with $q < 0$ [Figs. 24(a1–d1,a4–d4) and 24(a2–d2,a5–d5)], while $\langle \sigma_Q^x \sigma_{-Q}^x \rangle$ with $q > 0$ [Figs. 22(a3–d3,a6–d6)] are different from those with $q < 0$ [Figs. 24(a3–d3,a6–d6)]. These are consequences of the invariance of \mathcal{H}_0 . For $J_{3s,3}/J_{nn} = 0.1$ and at $T/J_{nn} = 0.2$, since the invariance does not hold for $J_{3s,3} \neq 0$, $S(\mathbf{Q})$ and $\langle \sigma_Q^z \sigma_{-Q}^z \rangle$ with $q > 0$ [Figs. 23(a1–d1,a2–d2)] are different from those with $q < 0$ [Figs. 25(a1–d1,a2–d2)].

In relation to the analysis of TTO, from experience in Secs. IVC 1–IV C 3 we think that the important parameters can be

found by inspection of $C(T)$ curves, i.e., by selecting $C(T)$ satisfying three conditions: $J_{3s,3}/J_{nn} = 0.1$, $q > 0$, temperature dependence of $C(T)$ is similar to that with $q = 0.5$ or 0.55 shown in Fig. 11(a). By inspecting Fig. 21(a), it is obvious that these conditions are met by three $C(T)$ curves with $J_{3s,3}/J_{nn} = 0.1$ and with $(\delta, q) = (0.1, 0.5)$, $(0.1, 0.4)$, and $(-0.1, 0.6)$, the points 22–24 in Fig. 1. The corresponding three 2D slices of $S(\mathbf{Q})$ at $T/J_{nn} = 0.2$ [Figs. 23(a1–c1)] show spin correlations with $\mathbf{k} \sim (\frac{1}{2}, \frac{1}{2}, \frac{1}{2})$, which resemble those shown in Figs. 13(b1–d1). Therefore, we conclude that the TPQ results suggest that the effective Hamiltonian minimally describing TTO is $\mathcal{H}_0 + \mathcal{H}_{3s}$ with $J_{3s,1} = J_{3s,2} = 0$, $J_{3s,3}/J_{nn} \sim 0.1$ (or -0.1) and the parameters (δ, q) in the region which is enclosed by the red dashed line in Fig. 1.

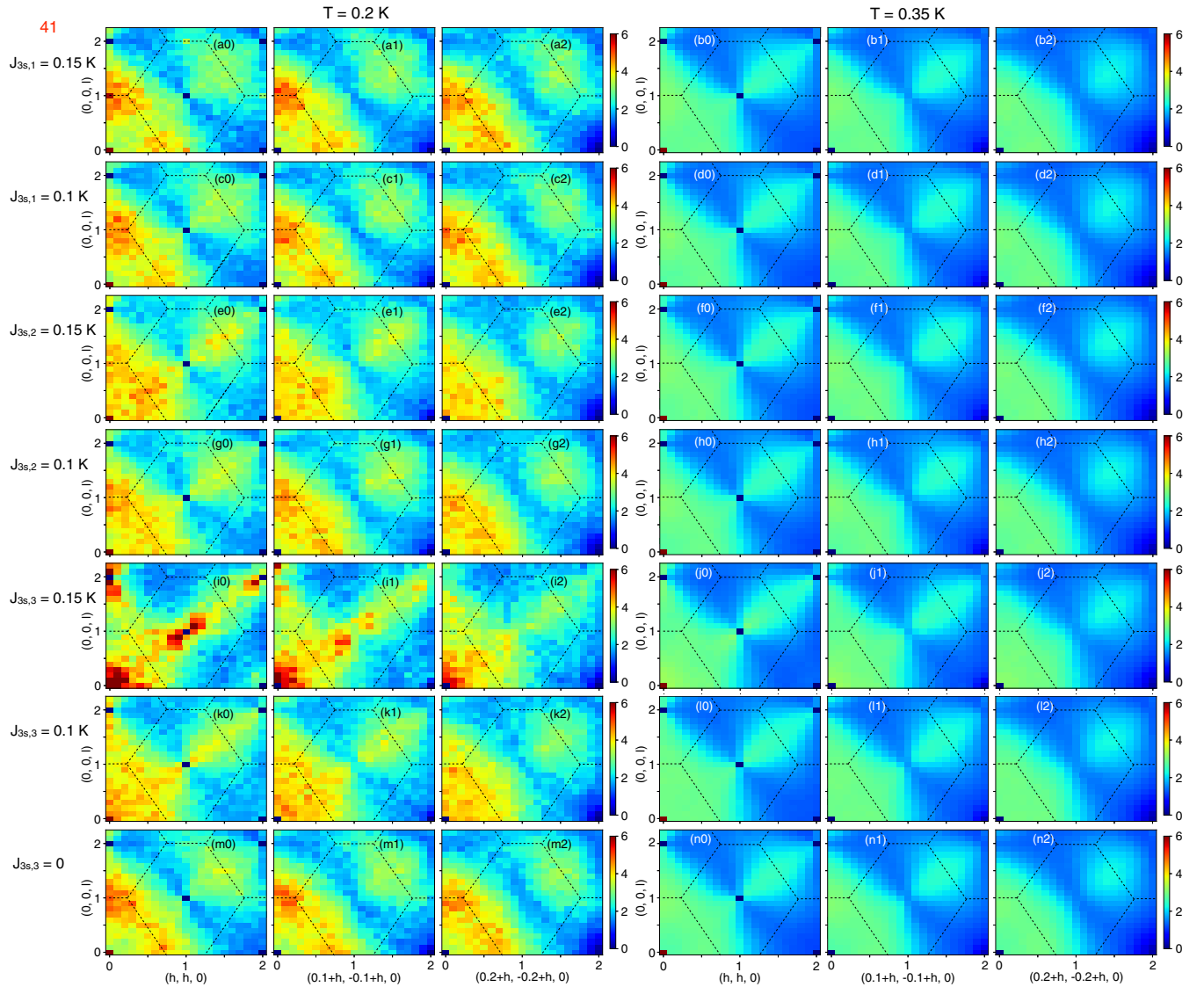


FIG. 19. Intensity maps of $S(\mathbf{Q})$ calculated by the 16000-site CMC simulations using parameters indicated by red circles shown in Figs. 7(e1–e3) ($J_{3s,i}$; $i = 1, 2, 3$; $J_{3s,j \neq i} = 0$) and by the point 41 in Fig. 3 [$\frac{J_{nn}}{J_{nn}+D_{nn}}(\delta, q) = (0.0, -0.45)$]. They are viewed by 2D slices of $\mathbf{Q} = (k + h, -k + h, l)$ with fixed $k = 0, 0.1$, and 0.2 , which are shown in (w0), (w1), and (w2) [$w=a-n$], respectively. They are calculated at two temperatures 0.2 K (a,c,e,g,i,k,m) and 0.35 K (b,d,f,h,j,l,n), below and above the specific-heat peak. Intensity maps for $J_{3s,1} = 0.15$ and 0.1 K [Fig. 7(b1)] are shown in (a,b) and (c,d), respectively. Intensity maps for $J_{3s,2} = 0.15$ and 0.1 K [Fig. 7(b2)] are shown in (e,f) and (g,h), respectively. Intensity maps for $J_{3s,3} = 0.15, 0.1$, and 0 K [Fig. 7(b3)] are shown in (i,j), (k,l), and (m,n), respectively.

We chose the eight parameter sets ($\delta = \pm 0.1, q$), the points 22–29 in Fig. 1: the two points 22 and 24 are in the 3D-PAF ($q > 0$) phase, the two points 26 and 28 are in the 3D-PAF ($q < 0$) phase, the four points 23, 25, 27, and 29 are in the SI phase because simulation results were expected to be similar to those of the four points 5, 7, 15, and 17 on the q axis ($\delta = 0$). But, this was not the case. For example, the intensity patterns of $\langle \sigma_{\mathbf{Q}}^x \sigma_{-\mathbf{Q}}^x \rangle$ with $(\delta, q) = (-0.1, 0.5)$ [Figs. 22(d3,d6) and 23(d3,d6)] and with $(\delta, q) = (-0.1, -0.5)$ [Figs. 24(d3,d6) and 25(d3,d6)] are very differ-

ent from those with $\delta = 0$. Since these seem to be caused by certain quantum corrections, simulations with systematic (δ, q) variation have to be performed to gain detailed information. Thus, instead of making further comments, we make two plausible remarks. A quantum correction would explain the reason why the region enclosed by red dashed line in Fig. 1 is not parallel to the classical phase boundary. All the results using the TPQ methods support that the $q < 0$ side of the phase diagram (Fig. 1) can be excluded from studies of TTO.

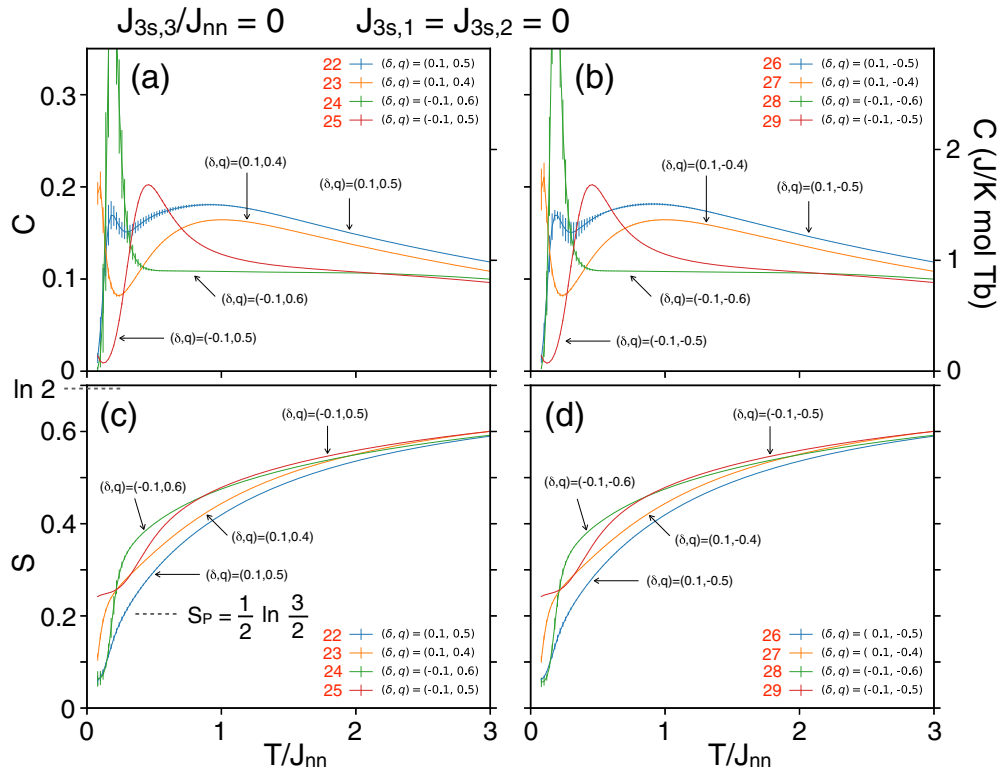


FIG. 20. Temperature dependence of specific heat $C(T)$ and entropy $S(T)$ obtained by the 32-site simulations using the cTPQ state for $J_{3s,3}/J_{nn} = 0$ ($J_{3s,1} = J_{3s,2} = 0$) with parameters ($\delta \neq 0, q$), the points 22–29 in Fig. 1. In (a) and (b) $C(T)$ for $q \geq 0$ and $q \leq 0$ are shown, respectively. In (c) and (d) $S(T)$ for $q \geq 0$ and $q \leq 0$ are shown, respectively.

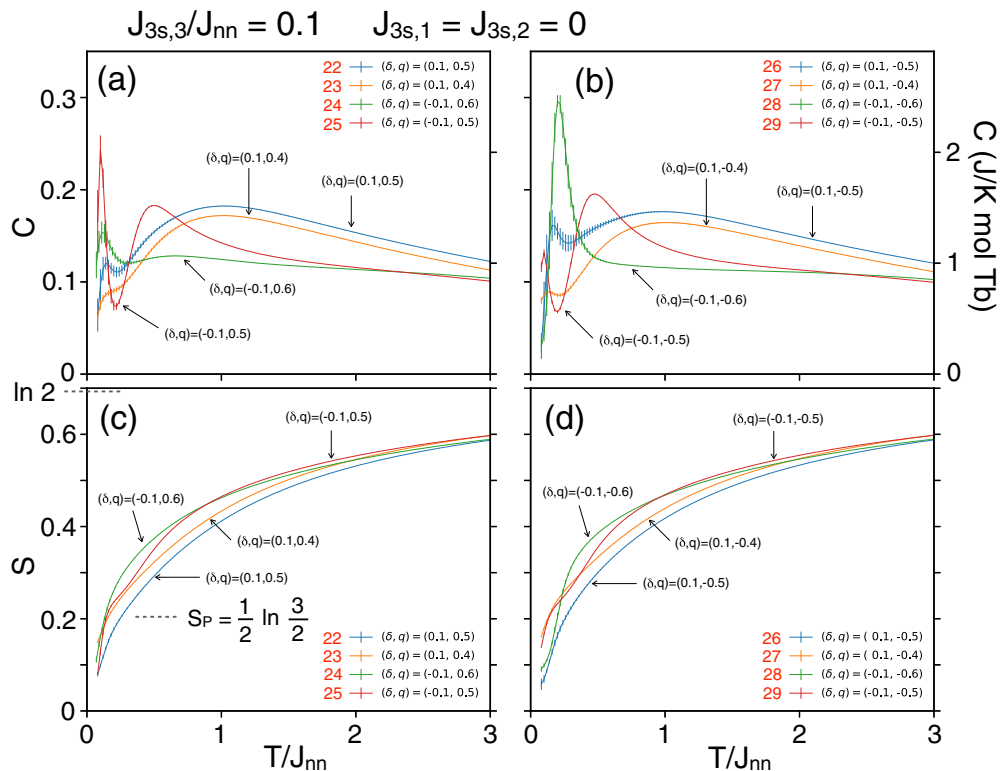


FIG. 21. Temperature dependence of specific heat $C(T)$ and entropy $S(T)$ obtained by the 32-site simulations using the cTPQ state for $J_{3s,3}/J_{nn} = 0.1$ ($J_{3s,1} = J_{3s,2} = 0$) with parameters ($\delta \neq 0, q$), the points 22–29 in Fig. 1. In (a) and (b) $C(T)$ for $q \geq 0$ and $q \leq 0$ are shown, respectively. In (c) and (d) $S(T)$ for $q \geq 0$ and $q \leq 0$ are shown, respectively.

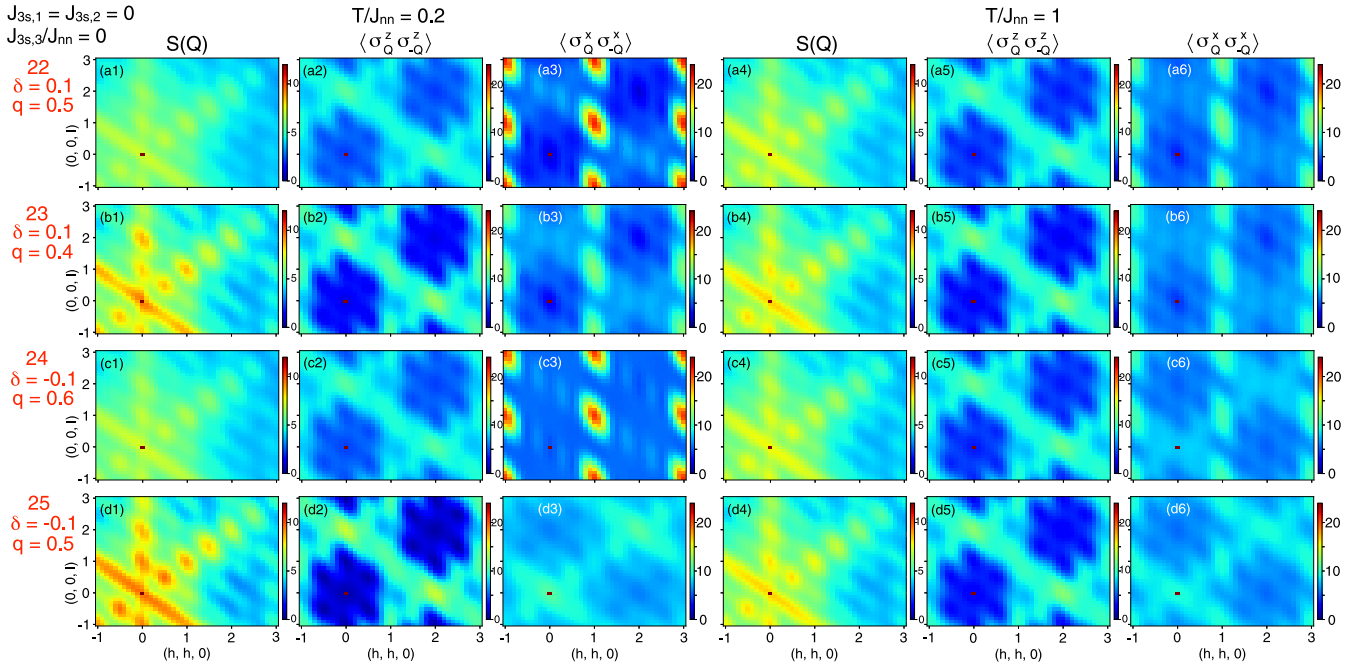


FIG. 22. Two-dimensional slices of (w1,w4) $S(\mathbf{Q})$, (w2,w5) $\langle \sigma_{\mathbf{Q}}^z \sigma_{-\mathbf{Q}}^z \rangle$, and (w3,w6) $\langle \sigma_{\mathbf{Q}}^x \sigma_{-\mathbf{Q}}^x \rangle$ [$w=a-d$] in the plane $\mathbf{Q} = (h, h, l)$ calculated by the 32-site simulations using the mTPQ state for $J_{3s,3}/J_{nn} = 0$ ($J_{3s,1} = J_{3s,2} = 0$) with parameters ($\delta = \pm 0.1, q > 0$), the points 22–25 in Fig. 1. The 2D slice data at $T/J_{nn} = 0.2$ and 1 are shown in (w1)–(w3) and (w4)–(w6) [$w=a-d$], respectively.

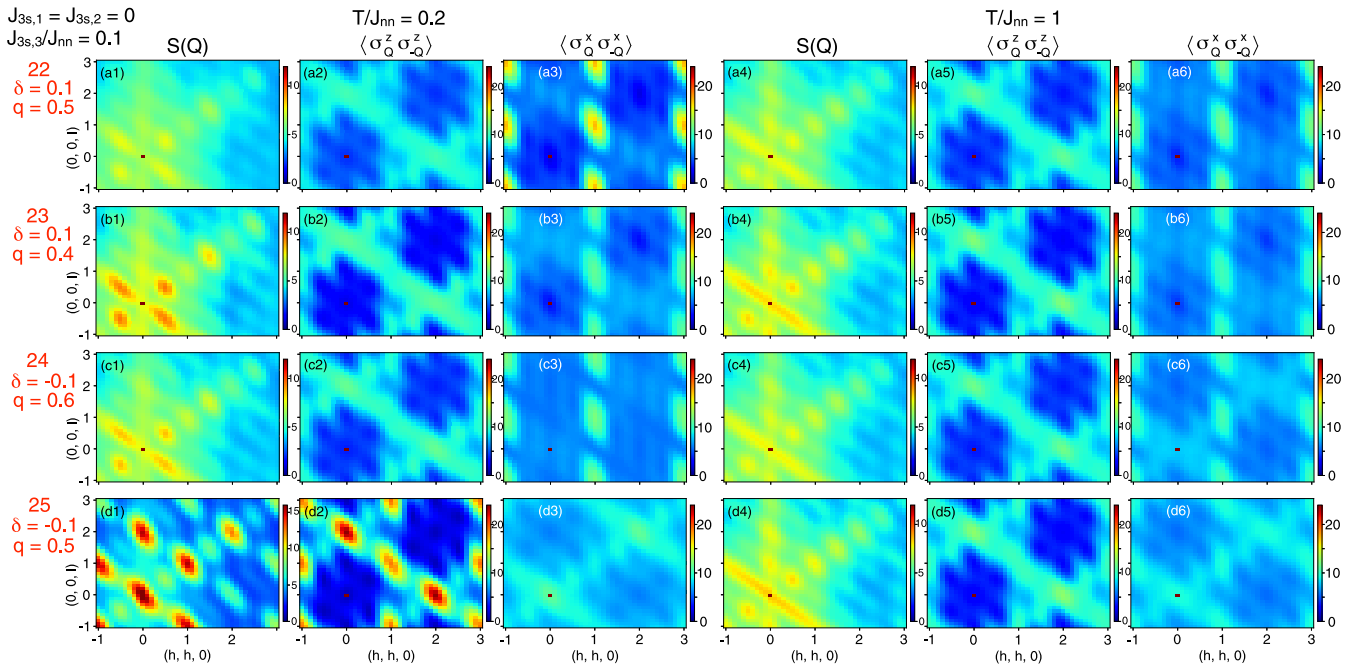


FIG. 23. Two-dimensional slices of (w1,w4) $S(\mathbf{Q})$, (w2,w5) $\langle \sigma_{\mathbf{Q}}^z \sigma_{-\mathbf{Q}}^z \rangle$, and (w3,w6) $\langle \sigma_{\mathbf{Q}}^x \sigma_{-\mathbf{Q}}^x \rangle$ [$w=a-d$] in the plane $\mathbf{Q} = (h, h, l)$ calculated by the 32-site simulations using the mTPQ state for $J_{3s,3}/J_{nn} = 0.1$ ($J_{3s,1} = J_{3s,2} = 0$) with parameters ($\delta = \pm 0.1, q > 0$), the points 22–25 in Fig. 1. The 2D slice data at $T/J_{nn} = 0.2$ and 1 are shown in (w1)–(w3) and (w4)–(w6) [$w=a-d$], respectively.

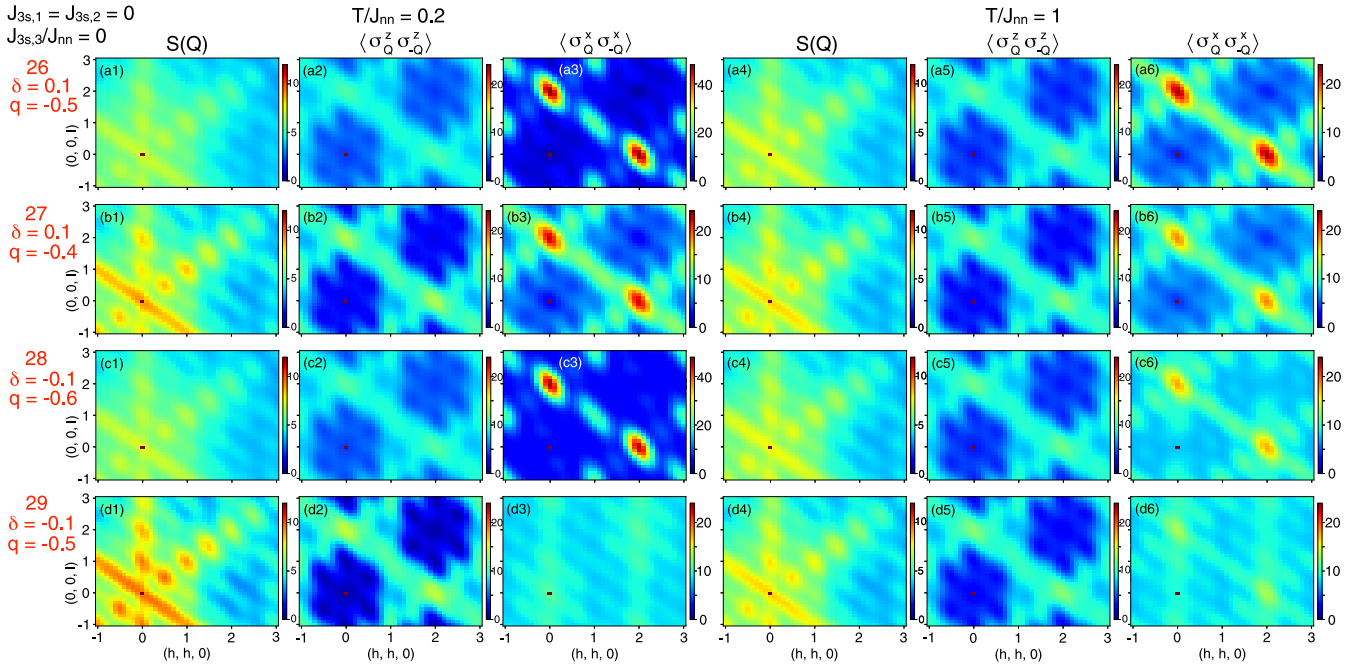


FIG. 24. Two-dimensional slices of (w1,w4) $S(Q)$, (w2,w5) $\langle \sigma_Q^z \sigma_{-Q}^z \rangle$, and (w3,w6) $\langle \sigma_Q^x \sigma_{-Q}^x \rangle$ [w=a-d] in the plane $Q = (h, h, l)$ calculated by the 32-site simulations using the mTPQ state for $J_{3s,3}/J_{nn} = 0$ ($J_{3s,1} = J_{3s,2} = 0$) with parameters ($\delta = \pm 0.1, q < 0$), the points 26–29 in Fig. 1. The 2D slice data at $T/J_{nn} = 0.2$ and 1 are shown in (w1)–(w3) and (w4)–(w6) [w=a–d], respectively.

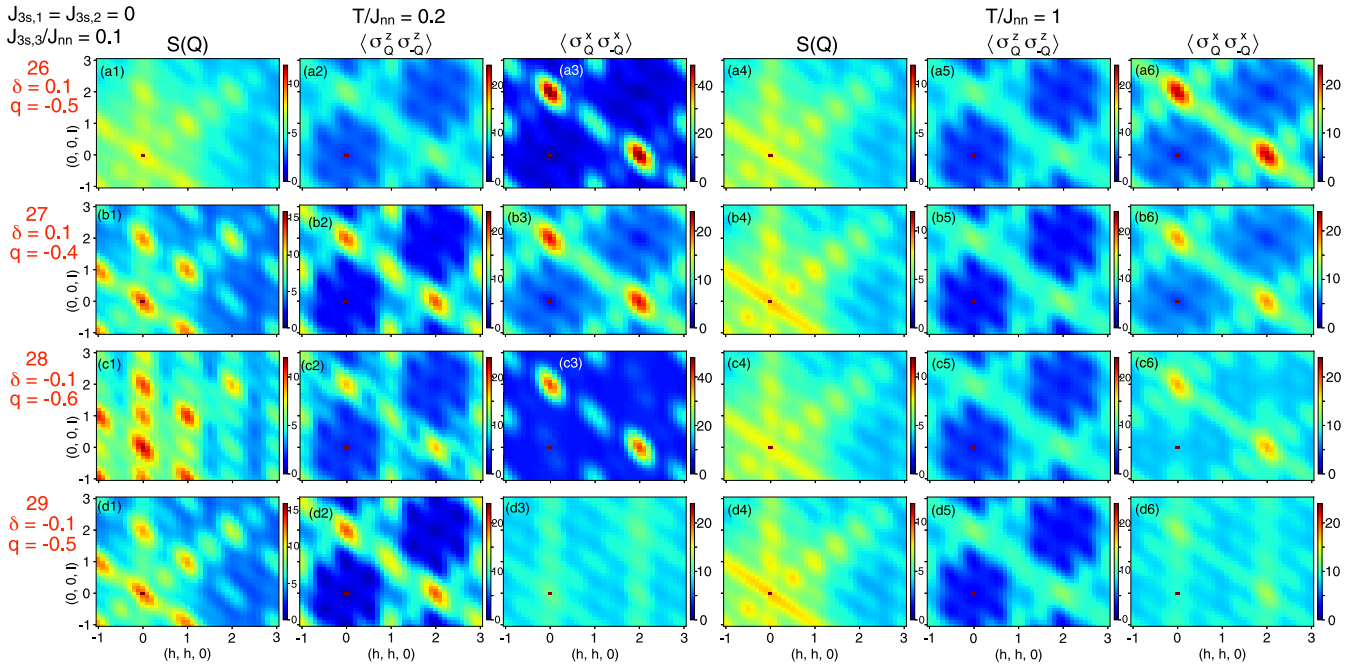


FIG. 25. Two-dimensional slices of (w1,w4) $S(Q)$, (w2,w5) $\langle \sigma_Q^z \sigma_{-Q}^z \rangle$, and (w3,w6) $\langle \sigma_Q^x \sigma_{-Q}^x \rangle$ [w=a–d] in the plane $Q = (h, h, l)$ calculated by the 32-site simulations using the mTPQ state for $J_{3s,3}/J_{nn} = 0.1$ ($J_{3s,1} = J_{3s,2} = 0$) with parameters ($\delta = \pm 0.1, q < 0$), the points 26–29 in Fig. 1. The 2D slice data at $T/J_{nn} = 0.2$ and 1 are shown in (w1)–(w3) and (w4)–(w6) [w=a–d], respectively.

- [1] *Introduction to Frustrated Magnetism*, edited by C. Lacroix, P. Mendels, and F. Mila (Springer, Berlin, 2011).
- [2] G. H. Wannier, Antiferromagnetism: The triangular ising net, *Phys. Rev.* **79**, 357 (1950).
- [3] M. Mekata, Antiferro-ferrimagnetic transition in triangular ising lattice, *J. Phys. Soc. Jpn.* **42**, 76 (1977).
- [4] K. Hirakawa, H. Kadowaki, and K. Ubukoshi, Experimental Studies of Triangular Lattice Antiferromagnets with $S = 1/2$: NaTiO_2 and LiNiO_2 , *J. Phys. Soc. Jpn.* **54**, 3526 (1985).
- [5] I. Syôzi, Statistics of Kagome Lattice, *Prog. Theor. Phys.* **6**, 306 (1951).
- [6] M. P. Shores, E. A. Nytko, B. M. Bartlett, and D. G. Nocera, A structurally perfect $S = 1/2$ Kagome antiferromagnet, *J. Am. Chem. Soc.* **127**, 13462 (2005).
- [7] T.-H. Han, J. S. Helton, S. Chu, D. G. Nocera, J. A. Rodriguez-Rivera, C. Broholm, and Y. S. Lee, Fractionalized excitations in the spin-liquid state of a kagome-lattice antiferromagnet, *Nature (London)* **492**, 406 (2012).
- [8] P. W. Anderson, Ordering and antiferromagnetism in ferrites, *Phys. Rev.* **102**, 1008 (1956).
- [9] J. S. Gardner, S. R. Dunsiger, B. D. Gaulin, M. J. P. Gingras, J. E. Greedan, R. F. Kiefl, M. D. Lumsden, W. A. MacFarlane, N. P. Raju, J. E. Sonier, I. Swainson, and Z. Tun, Cooperative Paramagnetism in the Geometrically Frustrated Pyrochlore Antiferromagnet $\text{Tb}_2\text{Ti}_2\text{O}_7$, *Phys. Rev. Lett.* **82**, 1012 (1999).
- [10] S. T. Bramwell and M. J. P. Gingras, Spin ice state in frustrated magnetic pyrochlore materials, *Science* **294**, 1495 (2001).
- [11] J. S. Gardner, M. J. P. Gingras, and J. E. Greedan, Magnetic pyrochlore oxides, *Rev. Mod. Phys.* **82**, 53 (2010).
- [12] C. Castelnovo, R. Moessner, and S. L. Sondhi, Magnetic monopoles in spin ice, *Nature (London)* **451**, 42 (2008).
- [13] H. Kadowaki, N. Doi, Y. Aoki, Y. Tabata, T. J. Sato, J. W. Lynn, K. Matsuhira, and Z. Hiroi, Observation of magnetic monopoles in spin ice, *J. Phys. Soc. Jpn.* **78**, 103706 (2009).
- [14] T. Fennell, P. P. Deen, A. R. Wildes, K. Schmalzl, D. Prabhakaran, A. T. Boothroyd, R. J. Aldus, D. F. McMorrow, and S. T. Bramwell, Magnetic coulomb phase in the spin ice $\text{Ho}_2\text{Ti}_2\text{O}_7$, *Science* **326**, 415 (2009).
- [15] D. J. P. Morris, D. A. Tennant, S. A. Grigera, B. Klemke, C. Castelnovo, R. Moessner, C. Czternasty, M. Meissner, K. C. Rule, J. U. Hoffmann, K. Kiefer, S. Gerischer, D. Slobinsky, and R. S. Perry, Dirac Strings and Magnetic Monopoles in the Spin Ice $\text{Dy}_2\text{Ti}_2\text{O}_7$, *Science* **326**, 411 (2009).
- [16] S. T. Bramwell, S. R. Giblin, S. Calder, R. Aldus, D. Prabhakaran, and T. Fennell, Measurement of the charge and current of magnetic monopoles in spin ice, *Nature (London)* **461**, 956 (2009).
- [17] P. W. Anderson, Resonating valence bonds: A new kind of insulator? *Mater. Res. Bull.* **8**, 153 (1973).
- [18] L. Balents, Spin liquids in frustrated magnets, *Nature (London)* **464**, 199 (2010).
- [19] M. Hermele, M. P. A. Fisher, and L. Balents, Pyrochlore photons: The $U(1)$ spin liquid in a $S = \frac{1}{2}$ three-dimensional frustrated magnet, *Phys. Rev. B* **69**, 064404 (2004).
- [20] L. Savary and L. Balents, Quantum spin liquids: A review, *Rep. Prog. Phys.* **80**, 016502 (2017).
- [21] R. Sibille, E. Lhotel, M. Ciomaga Hatnean, G. J. Nilsen, G. Ehlers, A. Cervellino, E. Ressouche, M. Frontzek, O. Zaharko, V. Pomjakushin, U. Stuhr, H. C. Walker, D. T. Adroja, H. Luetkens, C. Baines, A. Amato, G. Balakrishnan, T. Fennell, and M. Kenzelmann, Coulomb spin liquid in anion-disordered pyrochlore $\text{Tb}_2\text{Hf}_2\text{O}_7$, *Nat. Commun.* **8**, 892 (2017).
- [22] B. Fåk, S. Bieri, E. Canévet, L. Messio, C. Payen, M. Viaud, C. Guillot-Deudon, C. Darie, J. Ollivier, and P. Mendels, Evidence for a spinon Fermi surface in the triangular $S = 1$ quantum spin liquid $\text{Ba}_3\text{NiSb}_2\text{O}_9$, *Phys. Rev. B* **95**, 060402(R) (2017).
- [23] P.-L. Dai, G. Zhang, Y. Xie, C. Duan, Y. Gao, Z. Zhu, E. Feng, Z. Tao, C.-L. Huang, H. Cao, A. Podlesnyak, G. E. Granroth, M. S. Everett, J. C. Neuefeind, D. Voneshen, S. Wang, G. Tan, E. Morosan, X. Wang, H.-Q. Lin *et al.*, Spinon Fermi Surface Spin Liquid in a Triangular Lattice Antiferromagnet NaYbSe_2 , *Phys. Rev. X* **11**, 021044 (2021).
- [24] T. Taniguchi, H. Kadowaki, H. Takatsu, B. Fåk, J. Ollivier, T. Yamazaki, T. J. Sato, H. Yoshizawa, Y. Shimura, T. Sakakibara, T. Hong, K. Goto, L. R. Yaraskavitch, and J. B. Kycia, Long-range order and spin-liquid states of polycrystalline $\text{Tb}_{2+x}\text{Ti}_{2-x}\text{O}_{7+y}$, *Phys. Rev. B* **87**, 060408(R) (2013).
- [25] M. Wakita, T. Taniguchi, H. Edamoto, H. Takatsu, and H. Kadowaki, Quantum spin liquid and electric quadrupolar states of single crystal $\text{Tb}_{2+x}\text{Ti}_{2-x}\text{O}_{7+y}$, *J. Phys.: Conf. Ser.* **683**, 012023 (2016).
- [26] H. Kadowaki, M. Wakita, B. Fåk, J. Ollivier, S. Ohira-Kawamura, K. Nakajima, H. Takatsu, and M. Tamai, Continuum excitation and pseudospin wave in quantum spin-liquid and quadrupole ordered states of $\text{Tb}_{2+x}\text{Ti}_{2-x}\text{O}_{7+y}$, *J. Phys. Soc. Jpn.* **87**, 064704 (2018).
- [27] H. Takatsu, S. Onoda, S. Kittaka, A. Kasahara, Y. Kono, T. Sakakibara, Y. Kato, B. Fåk, J. Ollivier, J. W. Lynn, T. Taniguchi, M. Wakita, and H. Kadowaki, Quadrupole Order in the Frustrated Pyrochlore $\text{Tb}_{2+x}\text{Ti}_{2-x}\text{O}_{7+y}$, *Phys. Rev. Lett.* **116**, 217201 (2016).
- [28] H. Kadowaki, H. Takatsu, T. Taniguchi, B. Fåk, and J. Ollivier, Composite Spin and Quadrupole Wave in the Ordered Phase of $\text{Tb}_{2+x}\text{Ti}_{2-x}\text{O}_{7+y}$, *SPIN* **05**, 1540003 (2015).
- [29] H. Kadowaki, H. Takatsu, and M. Wakita, Dimensional change of the quadrupole order in pseudospin- $\frac{1}{2}$ pyrochlore magnets under magnetic field in the [111] direction, *Phys. Rev. B* **98**, 144410 (2018).
- [30] S. Onoda and Y. Tanaka, Quantum melting of spin ice: Emergent cooperative quadrupole and chirality, *Phys. Rev. Lett.* **105**, 047201 (2010).
- [31] S. Onoda and Y. Tanaka, Quantum fluctuations in the effective pseudospin- $\frac{1}{2}$ model for magnetic pyrochlore oxides, *Phys. Rev. B* **83**, 094411 (2011).
- [32] S. B. Lee, S. Onoda, and L. Balents, Generic quantum spin ice, *Phys. Rev. B* **86**, 104412 (2012).
- [33] Y. Gritsenko, S. Mombetsu, P. T. Cong, T. Stöter, E. L. Green, C. S. Mejjia, J. Wosnitza, M. Ruminy, T. Fennell, A. A. Zvyagin, S. Zherlitsyn, and M. Kenzelmann, Changes in elastic moduli as evidence for quadrupolar ordering in the rare-earth frustrated magnet $\text{Tb}_2\text{Ti}_2\text{O}_7$, *Phys. Rev. B* **102**, 060403(R) (2020).
- [34] H. Kadowaki, M. Wakita, B. Fåk, J. Ollivier, S. Ohira-Kawamura, K. Nakajima, and J. W. Lynn, Spin correlations of quantum spin liquid and quadrupole-ordered states of $\text{Tb}_{2+x}\text{Ti}_{2-x}\text{O}_{7+y}$, *Phys. Rev. B* **99**, 014406 (2019).
- [35] J. G. Rau and M. J. P. Gingras, Frustrated quantum rare-earth pyrochlores, *Annu. Rev. Condens. Matter Phys.* **10**, 357 (2019).
- [36] H. R. Molavian, M. J. P. Gingras, and B. Canals, Dynamically Induced Frustration as a Route to a Quantum Spin Ice State

- in $\text{Tb}_2\text{Ti}_2\text{O}_7$ via Virtual Crystal Field Excitations and Quantum Many-Body Effects, *Phys. Rev. Lett.* **98**, 157204 (2007).
- [37] M. J. P. Gingras and P. A. McClarty, Quantum spin ice: a search for gapless quantum spin liquids in pyrochlore magnets, *Rep. Prog. Phys.* **77**, 056501 (2014).
- [38] Y. Kato and S. Onoda, Numerical Evidence of Quantum Melting of Spin Ice: Quantum-to-Classical Crossover, *Phys. Rev. Lett.* **115**, 077202 (2015).
- [39] S. Guitteny, I. Mirebeau, P. Dalmas de Réotier, C. V. Colin, P. Bonville, F. Porcher, B. Grenier, C. Decorse, and S. Petit, Mesoscopic correlations in $\text{Tb}_2\text{Ti}_2\text{O}_7$ spin liquid, *Phys. Rev. B* **92**, 144412 (2015).
- [40] H. R. Molavian, P. A. McClarty, and M. J. P. Gingras, Towards an Effective Spin Hamiltonian of the Pyrochlore Spin Liquid $\text{Tb}_2\text{Ti}_2\text{O}_7$, [arXiv:0912.2957](https://arxiv.org/abs/0912.2957).
- [41] D. P. Landau and K. Binder, *A Guide to Monte Carlo Simulations in Statistical Physics* (Cambridge University Press, Cambridge, 2015).
- [42] M. E. Zhitomirsky, P. C. W. Holdsworth, and R. Moessner, Nature of finite-temperature transition in anisotropic pyrochlore $\text{Er}_2\text{Ti}_2\text{O}_7$, *Phys. Rev. B* **89**, 140403(R) (2014).
- [43] H. Yan, O. Benton, L. Jaubert, and N. Shannon, Theory of multiple-phase competition in pyrochlore magnets with anisotropic exchange with application to $\text{Yb}_2\text{Ti}_2\text{O}_7$, $\text{Er}_2\text{Ti}_2\text{O}_7$, and $\text{Er}_2\text{Sn}_2\text{O}_7$, *Phys. Rev. B* **95**, 094422 (2017).
- [44] S. Popescu, A. J. Short, and A. Winter, Entanglement and the foundations of statistical mechanics, *Nat. Phys.* **2**, 754 (2006).
- [45] S. Goldstein, J. L. Lebowitz, R. Tumulka, and N. Zanghì, Canonical Typicality, *Phys. Rev. Lett.* **96**, 050403 (2006).
- [46] F. Jin, D. Willsch, M. Willsch, H. Lagemann, K. Michielsen, and H. De Raedt, Random state technology, *J. Phys. Soc. Jpn.* **90**, 012001 (2021).
- [47] A. Hams and H. De Raedt, Fast algorithm for finding the eigenvalue distribution of very large matrices, *Phys. Rev. E* **62**, 4365 (2000).
- [48] S. Sugiura and A. Shimizu, Thermal Pure Quantum States at Finite Temperature, *Phys. Rev. Lett.* **108**, 240401 (2012).
- [49] S. Sugiura and A. Shimizu, Canonical Thermal Pure Quantum State, *Phys. Rev. Lett.* **111**, 010401 (2013).
- [50] M. Kawamura, K. Yoshimi, T. Misawa, Y. Yamaji, S. Todo, and N. Kawashima, Quantum lattice model solver HΦ, *Comput. Phys. Commun.* **217**, 180 (2017).
- [51] T. Shimokawa and H. Kawamura, Finite-temperature crossover phenomenon in the $S = 1/2$ antiferromagnetic heisenberg model on the Kagome lattice, *J. Phys. Soc. Jpn.* **85**, 113702 (2016).
- [52] Y. Yamaji, T. Suzuki, T. Yamada, S.-i. Suga, N. Kawashima, and M. Imada, Clues and criteria for designing a Kitaev spin liquid revealed by thermal and spin excitations of the honeycomb iridate Na_2IrO_3 , *Phys. Rev. B* **93**, 174425 (2016).
- [53] G. Sala, M. B. Stone, B. K. Rai, A. F. May, P. Laurell, V. O. Garlea, N. P. Butch, M. D. Lumsden, G. Ehlers, G. Pokharel, D. Mandrus, D. S. Parker, S. Okamoto, G. B. Halász, and A. D. Christianson, Van Hove singularity in the magnon spectrum of the antiferromagnetic quantum honeycomb lattice, *Nat. Commun.* **12**, 171 (2021).
- [54] T. Misawa and Y. Yamaji, Finite-temperature signatures of spin liquids in frustrated hubbard model, *J. Phys. Soc. Jpn.* **87**, 023707 (2018).
- [55] K. Uematsu and H. Kawamura, Randomness-Induced Quantum Spin Liquid Behavior in the $s = 1/2$ Random-Bond Heisenberg Antiferromagnet on the Pyrochlore Lattice, *Phys. Rev. Lett.* **123**, 087201 (2019).
- [56] R. Schäfer, I. Hagymási, R. Moessner, and D. J. Luitz, Pyrochlore $S = \frac{1}{2}$ Heisenberg antiferromagnet at finite temperature, *Phys. Rev. B* **102**, 054408 (2020).
- [57] O. Benton, L. D. C. Jaubert, R. R. P. Singh, J. Oitmaa, and N. Shannon, Quantum Spin Ice with Frustrated Transverse Exchange: From a π -Flux Phase to a Nematic Quantum Spin Liquid, *Phys. Rev. Lett.* **121**, 067201 (2018).
- [58] I. Hagymási, R. Schäfer, R. Moessner, and D. J. Luitz, Possible Inversion Symmetry Breaking in the $S = 1/2$ Pyrochlore Heisenberg Magnet, *Phys. Rev. Lett.* **126**, 117204 (2021).
- [59] B. C. den Hertog and M. J. P. Gingras, Dipolar interactions and origin of spin ice in ising pyrochlore magnets, *Phys. Rev. Lett.* **84**, 3430 (2000).
- [60] S. V. Isakov, R. Moessner, and S. L. Sondhi, Why Spin Ice Obeys the Ice Rules, *Phys. Rev. Lett.* **95**, 217201 (2005).
- [61] B. Fåk, H. Kadowaki, J. Ollivier, and M. Wakita, Quadrupole order of $\text{Tb}_{2+x}\text{Ti}_{2-x}\text{O}_{7+y}$, Institut Laue-Langevin (ILL), doi:10.5291/ILL-DATA.4-05-628 (2015).
- [62] B. Fåk, H. Kadowaki, and J. Ollivier, Quadrupole order of $\text{Tb}_{2+x}\text{Ti}_{2-x}\text{O}_{7+y}$, Institut Laue-Langevin (ILL) doi:10.5291/ILL-DATA.4-05-635 (2016).
- [63] H. Kadowaki, <https://github.com/kadowaki-h/AbsorptionFactorIN5>; <https://github.com/kadowaki-h/AbsorptionFactorAMATERAS>.
- [64] R. Ewings, A. Buts, M. Le, J. van Duijn, I. Bustinduy, and T. Perring, Horace: Software for the analysis of data from single crystal spectroscopy experiments at time-of-flight neutron instruments, *Nucl. Instrum. Methods Phys. Res., Sect. A* **834**, 132 (2016).
- [65] K. Hukushima and K. Nemoto, Exchange Monte Carlo method and application to spin glass simulations, *J. Phys. Soc. Jpn.* **65**, 1604 (1996).
- [66] H. Nishimori, Diagonalization program for quantum spin systems TITPACK Ver. 2, *Bussei Kenkyu* **56**, 494 (1991).
- [67] H. Nishimori, TITPACK Ver. 2, http://www.qa.iir.titech.ac.jp/~nishimori/titpack2_new/index-e.html; our simulation program using the TPQ states is based on this TITPACK Ver. 2.
- [68] J. Schnack, J. Schulenburg, and J. Richter, Magnetism of the $N = 42$ kagome lattice antiferromagnet, *Phys. Rev. B* **98**, 094423 (2018).
- [69] I. Mirebeau, A. Apetrei, J. Rodríguez-Carvajal, P. Bonville, A. Forget, D. Colson, V. Glazkov, J. P. Sanchez, O. Isnard, and E. Suard, Ordered Spin Ice State and Magnetic Fluctuations in $\text{Tb}_2\text{Sn}_2\text{O}_7$, *Phys. Rev. Lett.* **94**, 246402 (2005).
- [70] O. Benton, L. D. C. Jaubert, H. Yan, and N. Shannon, A spin-liquid with pinch-line singularities on the pyrochlore lattice, *Nat. Commun.* **7**, 11572 (2016).
- [71] A. M. Hallas, W. Jin, J. Gaudet, E. M. Tonita, D. Pomaranski, C. R. C. Buhariwalla, M. Tachibana, N. P. Butch, S. Calder, M. B. Stone, G. M. Luke, C. R. Wiebe, J. B. Kycia, M. J. P. Gingras, and B. D. Gaulin, Intertwined Magnetic Dipolar and Electric Quadrupolar Correlations in the Pyrochlore $\text{Tb}_2\text{Ge}_2\text{O}_7$, [arXiv:2009.05036](https://arxiv.org/abs/2009.05036).
- [72] P. Bonville, I. Mirebeau, A. Gukasov, S. Petit, and J. Robert, Tetragonal distortion yielding a two-singlet spin liquid in pyrochlore $\text{Tb}_2\text{Ti}_2\text{O}_7$, *Phys. Rev. B* **84**, 184409 (2011).

- [73] I. Mirebeau, I. N. Goncharenko, G. Dhalle, and A. Revcolevschi, Pressure and Field Induced Magnetic Order in the Spin Liquid $\text{Tb}_2\text{Ti}_2\text{O}_7$ as Studied by Single Crystal Neutron Diffraction, *Phys. Rev. Lett.* **93**, 187204 (2004).
- [74] M. Ruminy, S. Guitteny, J. Robert, L.-P. Regnault, M. Boehm, P. Steffens, H. Mutka, J. Ollivier, U. Stuhr, J. S. White, B. Roessli, L. Bovo, C. Decorse, M. K. Haas, R. J. Cava, I. Mirebeau, M. Kenzelmann, S. Petit, and T. Fennell, Magnetoelastic excitation spectrum in the rare-earth pyrochlore $\text{Tb}_2\text{Ti}_2\text{O}_7$, *Phys. Rev. B* **99**, 224431 (2019).
- [75] F. Jin, C. Liu, Y. Chang, A. Zhang, Y. Wang, W. Liu, X. Wang, Y. Sun, G. Chen, X. Sun, and Q. Zhang, Experimental Identification of Electric Dipoles Induced by Magnetic Monopoles in $\text{Tb}_2\text{Ti}_2\text{O}_7$, *Phys. Rev. Lett.* **124**, 087601 (2020).
- [76] Y. Yasui, M. Kanada, M. Ito, H. Harashina, M. Sato, H. Okumura, K. Kakurai, and H. Kadowaki, Static correlation and dynamical properties of Tb^{3+} -moments in $\text{Tb}_2\text{Ti}_2\text{O}_7$ –Neutron scattering study–, *J. Phys. Soc. Jpn.* **71**, 599 (2002).
- [77] T. Fennell, M. Kenzelmann, B. Roessli, M. K. Haas, and R. J. Cava, Power-Law Spin Correlations in the Pyrochlore Antiferromagnet $\text{Tb}_2\text{Ti}_2\text{O}_7$, *Phys. Rev. Lett.* **109**, 017201 (2012).
- [78] S. Petit, P. Bonville, J. Robert, C. Decorse, and I. Mirebeau, Spin liquid correlations, anisotropic exchange, and symmetry breaking in $\text{Tb}_2\text{Ti}_2\text{O}_7$, *Phys. Rev. B* **86**, 174403 (2012).
- [79] K. Fritsch, K. A. Ross, Y. Qiu, J. R. D. Copley, T. Guidi, R. I. Bewley, H. A. Dabkowska, and B. D. Gaulin, Antiferromagnetic spin ice correlations at $(\frac{1}{2}, \frac{1}{2}, \frac{1}{2})$ in the ground state of the pyrochlore magnet $\text{Tb}_2\text{Ti}_2\text{O}_7$, *Phys. Rev. B* **87**, 094410 (2013).
- [80] Y. Imry and S.-k. Ma, Random-Field Instability of the Ordered State of Continuous Symmetry, *Phys. Rev. Lett.* **35**, 1399 (1975).
- [81] A. Aharony, Y. Imry, and S.-k. Ma, Lowering of Dimensionality in Phase Transitions with Random Fields, *Phys. Rev. Lett.* **37**, 1364 (1976).
- [82] J. Jensen and A. R. Mackintosh, *Rare Earth Magnetism* (Clarendon, Oxford, 1991).
- [83] I. Mirebeau, P. Bonville, and M. Hennion, Magnetic excitations in $\text{Tb}_2\text{Sn}_2\text{O}_7$ and $\text{Tb}_2\text{Ti}_2\text{O}_7$ as measured by inelastic neutron scattering, *Phys. Rev. B* **76**, 184436 (2007).
- [84] H. Kusunose, Description of multipole in f-electron systems, *J. Phys. Soc. Jpn.* **77**, 064710 (2008).
- [85] H. Kadowaki, H. Takatsu, T. Taniguchi, B. Fåk, and J. Ollivier, Erratum: Composite Spin and Quadrupole Wave in the Ordered Phase of $\text{Tb}_{2+x}\text{Ti}_{2-x}\text{O}_{7+y}$ [SPIN 5, 1540003 (2015)], <https://github.com/kadowaki-h/erratum-SPIN-5-1540003-2015>; the error corrected version of [SPIN 5, 1540003 (2015)] can be downloaded from [arXiv:1505.00503](https://arxiv.org/abs/1505.00503).
- [86] S. Onoda, Effective quantum pseudospin-1/2 model for Yb pyrochlore oxides, *J. Phys.: Conf. Ser.* **320**, 012065 (2011).
- [87] K. A. Ross, L. Savary, B. D. Gaulin, and L. Balents, Quantum Excitations in Quantum Spin Ice, *Phys. Rev. X* **1**, 021002 (2011).